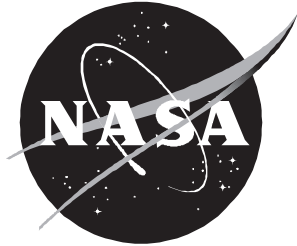


NASA/TP-1998-206908



Flow and Turbulence Modeling and Computation of Shock Buffet Onset for Conventional and Supercritical Airfoils

Robert E. Bartels
Langley Research Center, Hampton, Virginia

Corrected Copy

February 1998

The NASA STI Program Office . . . in Profile

Since its founding, NASA has been dedicated to the advancement of aeronautics and space science. The NASA Scientific and Technical Information (STI) Program Office plays a key part in helping NASA maintain this important role.

The NASA STI Program Office is operated by Langley Research Center, the lead center for NASA's scientific and technical information. The NASA STI Program Office provides access to the NASA STI Database, the largest collection of aeronautical and space science STI in the world. The Program Office is also NASA's institutional mechanism for disseminating the results of its research and development activities. These results are published by NASA in the NASA STI Report Series, which includes the following report types:

- **TECHNICAL PUBLICATION.** Reports of completed research or a major significant phase of research that present the results of NASA programs and include extensive data or theoretical analysis. Includes compilations of significant scientific and technical data and information deemed to be of continuing reference value. NASA counter-part or peer-reviewed formal professional papers, but having less stringent limitations on manuscript length and extent of graphic presentations.
- **TECHNICAL MEMORANDUM.** Scientific and technical findings that are preliminary or of specialized interest, e.g., quick release reports, working papers, and bibliographies that contain minimal annotation. Does not contain extensive analysis.
- **CONTRACTOR REPORT.** Scientific and technical findings by NASA-sponsored contractors and grantees.
- **CONFERENCE PUBLICATION.** Collected papers from scientific and technical conferences, symposia, seminars, or other meetings sponsored or co-sponsored by NASA.
- **SPECIAL PUBLICATION.** Scientific, technical, or historical information from NASA programs, projects, and missions, often concerned with subjects having substantial public interest.
- **TECHNICAL TRANSLATION.** English-language translations of foreign scientific and technical material pertinent to NASA's mission.

Specialized services that help round out the STI Program Office's diverse offerings include creating custom thesauri, building customized databases, organizing and publishing research results . . . even providing videos.

For more information about the NASA STI Program Office, see the following:

- Access the NASA STI Program Home Page at ***<http://www.sti.nasa.gov>***
- Email your question via the Internet to help@sti.nasa.gov
- Fax your question to the NASA Access Help Desk at (301) 621-0134
- Phone the NASA Access Help Desk at (301) 621-0390
- Write to:
NASA Access Help Desk
NASA Center for AeroSpace Information
800 Elkridge Landing Road
Linthicum Heights, MD 21090-2934

NASA/TP-1998-206908



Flow and Turbulence Modeling and Computation of Shock Buffet Onset for Conventional and Supercritical Airfoils

Robert E. Bartels
Langley Research Center, Hampton, Virginia

National Aeronautics and
Space Administration

Langley Research Center
Hampton, Virginia 23681-2199

February 1998

Available from the following:

NASA Center for AeroSpace Information (CASI)
800 Elkridge Landing Road
Linthicum Heights, MD 21090-2934
(301) 621-0390

National Technical Information Service (NTIS)
5285 Port Royal Road
Springfield, VA 22161-2171
(703) 487-4650

Contents

Symbols	v
Abstract	1
Introduction	1
Leading Order Matching and Boundary Layer Equations	3
Boundary Layer Turbulence Model Equations	5
Thin-Layer Navier-Stokes Turbulence Model Equations	8
Numerical Method for Interactive Boundary Layer Equations	9
Steady Computations	12
RAE 2822 Airfoil	12
NACA 64A010 Airfoil	17
NACA 0012 Airfoil	18
Unsteady Computations	21
NASA SC(2)-0714 Airfoil	21
NACA 0012 Airfoil	27
Concluding Remarks	30
References	32

Symbols

c^*	chord
c_f	friction coefficient
c_l	lift coefficient
c_p	pressure coefficient
$ \hat{c}_p $	Fourier transform modulus of c_p , Hz^{-2}
F	Levy-Lees streamwise velocity
F_{\pm}	scaled airfoil surface height, $f_{\pm} = \epsilon F_{\pm}$
F_1	k - ω and ϵ turbulence model blending function
f	reduced frequency, $\frac{\pi f^* c^*}{U_{\infty}^*}$
f_{\pm}	airfoil surface height
$f_{\pm t}$	airfoil surface velocity
$f_{\pm x}$	airfoil surface slope
f^*	frequency, Hz
k	turbulence kinetic energy, $\frac{1}{2}[\langle(u')^2\rangle + \langle(v')^2\rangle]$
M	Mach number
P_k	turbulence kinetic energy production due to mean rate of strain
P_{ω}	turbulence dissipation rate production due to mean rate of strain
p	pressure
R_{ij}	Reynolds stress tensor
R_1, \dots	boundary layer density perturbations
Re	Reynolds number
S_{ij}	mean velocity rate of strain tensor
T	temperature
t	time
U_1, \tilde{V}_1, \dots	boundary layer velocity perturbations
U_{∞}	free-stream velocity
u_e	boundary layer edge velocity
u_{τ}	friction velocity
$\langle u'v' \rangle$	Reynolds shear stress
$\langle (u')^2 \rangle, \langle (v')^2 \rangle$	Reynolds normal stresses
V	Levy-Lees normal velocity component
x, y	coordinates nondimensionalized by chord
Y	scaled boundary layer coordinate
α	angle of attack
α_l	boundary layer growth factor, 2ξ
β_n	turbulence model coefficient sets 1 and 2
γ_n	k - ω turbulence model coefficient
δ	boundary layer displacement thickness
δ_{ij}	Kroneker delta
δ_1	scaled boundary layer displacement thickness
ϵ	boundary layer expansion parameter, $O(\text{Re}^{-1/2})$ as $\text{Re} \rightarrow \infty$
η	boundary layer normal coordinate
Θ_1, \dots	boundary layer temperature perturbations
θ	Levy-Lees temperature
μ	molecular viscosity
μ_T	eddy viscosity
ν_T	kinematic eddy viscosity
ξ	boundary layer streamwise coordinate

ρ	density
$\sigma_{k,n}$	dissipation coefficient for turbulence kinetic energy equation
$\sigma_{\omega,n}$	dissipation coefficient for turbulence dissipation rate equation
τ	Reynolds stress
τ_w	wall shear
ϕ	perturbation velocity potential
φ_n	coefficients for turbulence models 1 and 2 blending
Ω	boundary layer vorticity
ω	specific turbulence dissipation rate

Subscripts:

ave	average
comp	computed
e	boundary layer edge
exp	experimental
min	minimum
∞	free-stream value
\pm	upper, lower surface

Superscript:

*	dimensional value
---	-------------------

Abbreviations:

b.l.	boundary layer
CAP	Computational Aeroelasticity Program
IBL	interactive boundary layer
J-K	Johnson-King
N-S	Navier-Stokes
SA	Spalart-Allmaras
SST	shear stress transport
TLNS	thin-layer Navier-Stokes
TSD	transonic small disturbance

Abstract

Flow and turbulence models applied to the problem of shock buffet onset are studied. The accuracy of the interactive boundary layer and the thin-layer Navier-Stokes equations solved with recent upwind techniques using similar transport field equation turbulence models is assessed for standard steady test cases, including conditions having significant shock separation. The two methods are found to compare well in the shock buffet onset region of a supercritical airfoil that involves strong trailing-edge separation. A computational analysis using the interactive boundary layer has revealed a Reynolds scaling effect in the shock buffet onset of the supercritical airfoil, which compares well with experiment. The methods are next applied to a conventional airfoil. Steady shock-separated computations of the conventional airfoil with the two methods compare well with experiment. Although the interactive boundary layer computations in the shock buffet region compare well with experiment for the conventional airfoil, the thin-layer Navier-Stokes computations do not. These findings are discussed in connection with possible mechanisms important in the onset of shock buffet and the constraints imposed by current numerical modeling techniques.

Introduction

Shock buffet or shock-induced oscillation (SIO) is large-scale flow-induced shock motion that involves alternating separation and reattachment of a boundary layer. In several recent computational studies, prominent features of the shock buffet of the 18-percent-thick circular-arc airfoil have been computed with Navier-Stokes and thin-layer Navier-Stokes codes (refs. 1 and 2). Those studies highlighted the sensitivity of this problem to the type of turbulence and flow model and the importance of shock and trailing-edge separation in the onset of shock buffet. Although details of the shock buffet are sensitive to these factors, all computations have computed the onset Mach number for the circular-arc airfoil quite accurately. After the comprehensive time accurate calculations made for the shock buffet of the 18-percent circular-arc airfoil in reference 2, an assessment using current methods and turbulence models of predictive capabilities for several more widely used airfoils was undertaken. The present report shows the results of a computational study of this problem with both the interactive boundary layer (IBL) method and a thin-layer Navier-Stokes (TLNS) code.

The physical mechanisms important in this problem can be investigated from a variety of viewpoints. For instance, shock strength is implicated in the identification of a Mach number range ahead of the shock for the 14-percent circular-arc airfoil in which shock buffet occurs (ref. 3). Geometry and trailing-edge viscous-inviscid interaction play a role as well. The 18-percent circular-arc airfoil has trailing-edge separation prior to shock separation and shock buffet onset (ref. 4). Trailing-edge separation has long been associated with the onset of shock buffet. (See refs. 5 and 6.) Shock buffet for this airfoil is antisymmetric and displays hysteresis in the onset Mach number range, the latter of which is discussed in reference 7 in connection with the coalescing of a shock and trailing-edge separation. Questions remain, however, as to the important mechanisms involved for other airfoils. For instance, the NACA 0012 airfoil has a much weaker trailing-edge separation in the onset region and experiences one-sided shock buffet (ref. 8). Nor does onset for this airfoil have a hysteresis in Mach number, and it does not apparently display the sensitivity of the shock buffet range on Reynolds number that is evident for the 18-percent circular-arc airfoil (ref. 8).

Experimental measurement of shock buffet onset is of course complicated by external effects such as wind tunnel noise, Reynolds scaling, and walls. However, experiment and several computations show transonic Mach numbers within an angle-of-attack envelope for the NACA 0012 airfoil where shock motion intensity and chordwise extent change from a localized shock oscillatory (or steady in the case of the computations) to a large-scale motion displaying limit cycle behavior. This has been studied experimentally for the NACA 0012 airfoil in reference 8, which represents an effort to provide quality steady and unsteady lifting surface results with minimal interference effects. In the test of reference 8, tunnel walls were contoured to match free air streamlines for nominal test conditions derived from Navier-Stokes computations. A much less extensive study of the NACA 0012 airfoil has been presented in reference 9, which also reveals shock buffet behavior. Reference 10, in contrast, presents experimental data from a slotted-wall wind tunnel for the same airfoil and range of conditions that are steady. Experimental studies through the onset Mach number range for several supercritical airfoils confirm that these airfoils can also experience shock buffet (refs. 9, 11, 12, and 13). In summary, although difficulties remain in verifying onset and sorting out the various extraneous effects, it is clear that under the right conditions some conventional and supercritical airfoils experience shock buffet.

The computations vary somewhat for airfoils other than the 18-percent circular arc. Steady interactive boundary layer and Navier-Stokes solutions of the NACA 0012 airfoil have been previously published (e.g., refs. 14 and 15) and compared with the steady data of reference 10. Shock buffet interactive boundary layer computations for the same airfoil have been shown in previous publications with a time accurate integral boundary layer and the classical transonic small disturbance (TSD) equation (ref. 16) and a TSD using an Euler-like streamwise flux and a steady integral boundary layer (ref. 7). This last reference has identified the onset behavior for the NACA 0012 airfoil as a Hopf bifurcation point where the solution changes from an equilibrium point to a limit cycle solution. The critical point or onset location is the point having a zero amplitude limit cycle solution. Whether a supercritical airfoil behaves like a conventional airfoil or like the 18-percent circular-arc airfoil in this and other respects, however, remains to be ascertained. But the fact that the interactive boundary layer approach has given shock buffet onset for the NACA 0012 airfoil that compares well with the onset of reference 8 (e.g., refs. 7 and 17) encourages one to pursue further investigation with this method. Although it is generally accepted that the boundary layer assumption is violated in many problems of this type, the interactive boundary layer method does make possible a broader study of the problem due to its efficiency. That is done here with a recently developed interactive boundary layer method using the CAP-TSD (Computational Aeroelasticity Program) potential code with a modified streamwise flux (ref. 18) and an unsteady compressible boundary layer solved in finite difference form. This method is shown to give very accurate results for many widely used attached and shock-separated steady test conditions. Comparisons of wall shear, boundary layer velocity profiles, and pressure distributions are shown to match well with experiment and Navier-Stokes results. In view of the sensitivity of the 18-percent circular-arc airfoil shock buffet to turbulence and flow model, comparisons of shock buffet onset for the NACA 0012 airfoil using several turbulence models are shown. Results are presented for several variations of the $k-\omega$ turbulence model. The $k-\omega$ turbulence model embodies more flow physics than one- or zero-equation turbulence models and is applicable to boundary layer dominated flows. It allows solution of the turbulence equations to the wall including the viscous sublayer and also allows modeling of free-stream turbulence and the effect of varying surface roughnesses. This allows the effect of these modeling parameters on shock buffet onset to be investigated. The shear stress transport form of the model is used to compute details of the shock buffet of the NASA SC(2)-0714 airfoil (ref. 13). Comparisons with the experimental shock buffet data at high Reynolds numbers of reference 13 are shown at several Reynolds numbers; this represents the first numerical study of the effect of turbulent boundary layer Reynolds number scaling on shock

buffet onset. The wind tunnel walls are not modeled computationally, and wind tunnel effects are only considered when using standard corrections to Mach number and angle of attack.

Previous unsteady thin-layer Navier-Stokes shock buffet results for a conventional and supercritical airfoil using the Baldwin-Lomax model and flux differences using artificial smoothing were shown by other authors in references 9 and 19. In the present effort, the Navier-Stokes simulation of shock buffet flows about these airfoils is made with Roe's upwind split flux differencing and an advanced turbulence model. Thin-layer Navier-Stokes computations are shown using the Menter $k-\omega$ shear stress transport (SST) and the Spalart-Allmaras (SA) turbulence models. Thin-layer Navier-Stokes results with a steady separated shock are shown that compare well with the steady interactive boundary layer results; these are followed with thin-layer Navier-Stokes computations in the shock buffet onset regions of the two airfoils. The effect of transition location in the shock buffet onset region of the NACA 0012 airfoil is also examined.

First, the equations and some pertinent theory behind the methods and turbulence models used in this study are given. Then, the numerical method of the interactive boundary layer model is described. Last, computational results and comparisons with experiment are presented.

Leading Order Matching and Boundary Layer Equations

As the starting point for obtaining the boundary layer equations, the Navier-Stokes equations are nondimensionalized by the airfoil chord c^* and the free-stream density, velocity, and viscosity, denoted by ρ_∞^* , U_∞^* , and μ_∞^* , respectively. Nondimensional variables are defined by

$$\begin{aligned} t &= \frac{t^* U_\infty^*}{c^*} & x &= \frac{x^*}{c^*} & y &= \frac{y^*}{c^*} \\ u &= \frac{u^*}{U_\infty^*} & v &= \frac{v^*}{U_\infty^*} & T &= \frac{T^*}{T_\infty^*} \\ \rho &= \frac{\rho^*}{\rho_\infty^*} & p &= \frac{p^* - p_\infty^*}{\rho_\infty^* U_\infty^{*2}} & \mu &= \frac{\mu^*}{\mu_\infty^*} \end{aligned}$$

where u is nondimensional x -velocity component and v is nondimensional y -velocity component. Because of the dependence of the resulting equations on Reynolds number, $Re = \rho_\infty^* U_\infty^* c^* / \mu_\infty^*$, the unsteady compressible boundary layer equations may be obtained upon expansion of quantities in terms of successively smaller orders of the parameter ϵ . The boundary layer vertical scale is defined by $y = \epsilon Y$, for a constant y as $\epsilon \rightarrow 0$ and streamwise extent of $O(1)$. In the boundary layer, expansions for velocities, pressure, density, temperature, and displacement thickness are

$$\begin{aligned} u &\sim U_1 + \epsilon U_2 + \dots & v &\sim \epsilon \tilde{V}_1 + \epsilon^2 \tilde{V}_2 + \dots \\ p &\sim P_1 + \epsilon P_2 + \dots & \rho &\sim R_1 + \epsilon R_2 + \dots \\ T &\sim \Theta_1 + \epsilon \Theta_2 + \dots & \delta &\sim \epsilon \delta_1 + \dots \end{aligned}$$

Displacement thickness is defined here as

$$\delta_1 = \int_0^\infty 1 - \left(\frac{R_1 U_1}{\rho_e u_e} \right) dY$$

where the subscript e refers to values at the boundary layer edge. To match with the boundary layer, outer flow quantities are expanded as

$$\begin{aligned}
u &\sim u_1 + \epsilon u_2 + \dots & v &\sim v_1 + \epsilon v_2 + \dots \\
p &\sim p_1 + \epsilon p_2 + \dots & \rho &\sim \rho_1 + \epsilon \rho_2 + \dots \\
T &\sim T_1 + \epsilon T_2 + \dots
\end{aligned}$$

For the present purpose of obtaining equations usable in solving an airfoil problem, the boundary layer equations are Favre mass averaged and then Prandtl transposed. The coordinate and velocity definitions are $Y = \pm Y_{\pm} + F_{\pm}(x, t)$ and $\tilde{V}_1 = \pm V + U_1 F_{\pm x} + F_{\pm t}$ for the upper and lower surface boundary layers, respectively. Here the airfoil surface height is defined as $f_{\pm} = \epsilon F_{\pm}$. The boundary layer equations remain unchanged in form, whereas the inviscid velocity injection after transformation has the changes to be noted subsequently.

The equations are transformed using Levy-Lees variables. The transformation is

$$\xi = x \quad \eta_{\pm} = \frac{1}{\sqrt{\alpha_l}} \int_0^{Y_{\pm}} R_1 d\tilde{Y}$$

and

$$\begin{aligned}
F &= U_1 & V &= -\sqrt{\alpha_l} \frac{\partial}{\partial \xi} \left(\sqrt{\alpha_l} \int_0^{Y_{\pm}} F d\eta \right) \\
p &= P_1 & \theta &= \Theta_1
\end{aligned}$$

where $\alpha_l = 2\xi$. The boundary layer equations become

$$\left. \begin{aligned}
V_{\eta} + F + \alpha_l F_{\xi} &= 0 \\
[(l + l_T)F_{\eta}]_{\eta} - \frac{\alpha_l}{\rho_e \theta_e} \theta p_{\xi} - V F_{\eta} - \alpha_l F_t + F V_{\eta} + F^2 &= 0 \\
p_{\eta} &= 0
\end{aligned} \right\} \quad (1)$$

In these equations $l = \rho\mu$ and $l_T = \rho\mu_T$, where μ is molecular viscosity and μ_T is eddy viscosity.

The complete set of adiabatic wall boundary conditions at $\eta_{\pm} = 0$ are $F = V = 0$, $p_{\eta_{\pm}} = 0$, and $\theta_{\eta} = 0$. In the wake, the boundary condition is $F_{\eta_{\pm}} = 0$ for a symmetric wake at $\eta_{\pm} = 0$, whereas an additional equation, such as ξ -momentum, would be required for an asymmetric wake.

The leading order matching conditions can be rewritten as

$$F(\xi, \eta_{\pm}, t) = u_1(x, 0_{\pm}, t) = 1 + \phi_x(x, 0_{\pm}, t) \quad (2)$$

$$V - \eta_{\pm} V_{\eta} = \sqrt{\alpha_l} \frac{d}{d\xi} [\rho_e u_e (\delta_1 + \tilde{\theta})] \quad (3)$$

as $\eta_{\pm} \rightarrow \infty$ and

$$\left. \begin{aligned}
p(\xi, t) &= p_1(x, 0_{\pm}, t) \\
\theta(\xi, \eta_{\pm}, t) &= T_1(x, 0_{\pm}, t)
\end{aligned} \right\} \quad (4)$$

where $(u, v) = \nabla\phi$. In equation (3), $\tilde{\theta} = \frac{\sqrt{\alpha_l}}{\rho_e} \int_0^{\eta_{\pm}} (1 - \theta) d\eta$. The leading order inviscid injection velocity is now

$$\phi_y(x, 0_{\pm}, t) = \epsilon \left\{ \pm \frac{d(\rho_e u_e \delta_1)}{dx} \mp \int_0^{Y_{\pm}} [R_{1t}(x, \tilde{Y}, t) - \rho_{1t}(x, 0, t)] d\tilde{Y} \right\} \rho_e^{-1} + f_{\pm x} + f_{\pm t} \quad (5)$$

as $Y_{\pm} \rightarrow \infty$. The plus and minus in equation (5) refer to the upper and lower surfaces, respectively. In the computations that follow we set $f_{\pm t} = 0$.

Boundary Layer Turbulence Model Equations

Variables are nondimensionalized in a manner identical to the boundary layer equations, with turbulence kinetic energy and specific dissipation rate nondimensionalized by U_{∞}^{*2} and U_{∞}^*/c^* , respectively. The resulting equations are Favre mass averaged and the nondimensional k - ω equations rescaled in the same way as the boundary layer equations with the largest order terms retained. The equations are transformed with a steady Prandtl transposition given in the previous section.

Transformation with boundary layer variables defined in previous section brings the equations into a nonasymptotic nonsimilarity form that is compatible with the boundary layer equations. The form of the equations is

$$\frac{dk}{dt} = \tilde{P}_k - \alpha_l \beta^* \omega k + \frac{\partial}{\partial \eta} \left[(l + \sigma_{k,n} l_T) \frac{\partial k}{\partial \eta} \right] \quad (6a)$$

$$\frac{d\omega}{dt} = \tilde{P}_{\omega} - \alpha_l \beta_n \omega^2 + 2 \text{Re} \sigma_{\omega,n} \frac{1}{\omega} \frac{\partial k}{\partial \eta} \frac{\partial \omega}{\partial \eta} F_1 + \frac{\partial}{\partial \eta} \left[(l + \sigma_{\omega,n} l_T) \frac{\partial \omega}{\partial \eta} \right] \quad (6b)$$

where the transformed convective derivative is defined $d()/dt = \alpha_l (\partial/\partial t + F \partial/\partial \xi) + V \partial/\partial \eta$. The first two terms on the right, \tilde{P}_k and \tilde{P}_{ω} , are transformed turbulence production due to mean flow gradients with Reynolds stresses replaced by using the Boussinesq approximation. The tensor form of the production terms (in terms of physical quantities) is given by

$$\left. \begin{aligned} P_k &= R_{ij} \frac{\partial U_j}{\partial x_i} \\ R_{ij} &= \nu_T S_{ij} - \frac{2}{3} k \delta_{ij} \\ P_{\omega} &= \gamma_n \frac{\partial U_j}{\partial x_i} \end{aligned} \right\} \quad (7)$$

where S_{ij} is the mean velocity rate of strain tensor and R_{ij} is the modeled Reynolds stress. In this study, only the leading order boundary layer production terms have been retained. Furthermore, transformation of these equations results in velocity as well as density gradient terms arising from the normal Reynolds stress production term. The part of this production term involving density gradient has also been neglected to simplify the expression; this is justified because the effect of density gradients is expected to be relatively small in the present transonic applications. Also, in many models, the effect of the normal Reynolds stress production is neglected altogether, although in the present implementation the contribution due to velocity gradient has been retained. This is based on the observation of Delery from experimental data: this contribution due to velocity gradient can become important in shock separating flows. (See ref. 20.) The remaining terms on the right of equations (6) result from diffusion and dissipation. After solution of the complete equation set, the eddy viscosity is found by $\nu_T = \text{Re} k/\omega$. Note that this equation set treats eddy viscosity as a scalar quantity and, therefore, does not correctly incorporate the relationship between $\langle (v')^2 \rangle$ and $\langle (u')^2 \rangle$; this can be important at a shock separation.

Variations of the k - ω turbulence model can be created from equations (6) by using different sets of coefficients. The three variations of the k - ω turbulence model and the coefficients used in each is summarized in table 1. The first variation is the Wilcox k - ω model (with F_1 in

Table 1. Coefficients for Boundary Layer Two-Equation Turbulence Model

Model	n	$\sigma_{k,n}$	$\sigma_{\omega,n}$	β_n
$k-\omega$	1	0.5	0.500	0.750
$k-\omega/k-\epsilon$	1	0.5	0.500	0.750
	2	1.0	0.856	0.828
SST	1	0.85	0.650	0.750
	2	1.00	0.856	0.828

equations (6) set to 0). The second set is the $k-\omega/k-\epsilon$ model. In this variant the $k-\omega$ model is used near the wall, whereas the $k-\epsilon$ model is used in the outer boundary layer. The $k-\epsilon$ model is activated by the factor F_1 in equation (6b) (with $F_1 = 1$). The coefficients of this two-layer variation are

$$\left. \begin{aligned} \sigma_{k,1} &= 0.5 & \sigma_{\omega,1} &= 0.500 & \beta_1 &= 0.0750 \\ \sigma_{k,2} &= 1.0 & \sigma_{\omega,2} &= 0.856 & \beta_2 &= 0.0828 \\ \beta^* &= 0.09 & \kappa &= 0.41 \\ \gamma_n &= \beta_n/\beta^* - \sigma_{\omega,n} \kappa^2/\sqrt{\beta^*} \end{aligned} \right\} \quad (8)$$

for $n=1,2$. The $k-\omega$ model (first variation) uses the first set of coefficients ($n = 1$). In the two-layer model ($k-\omega/k-\epsilon$), the coefficients of equations (8) are blended from layer 1 to 2 by using the function

$$\varphi = (1 - F_1)\varphi_1 + F_1\varphi_2 \dots \quad (\varphi_n = (\sigma_{k,n}, \sigma_{\omega,n}, \beta_n, \gamma_n))$$

The blending function is determined from $F_1 = \frac{1}{2}[1 + \tanh(\arg_1)]$. Menter and Rumsey give a function for \arg_1 involving variables y, ω, ν, k , and other constants. (See ref. 21.) In the present method a simple expression is used based on boundary layer thickness that maintains a nearly constant relative location (at approximately the center of the boundary layer) and width of the transitional region. The blending function for several representative velocity profiles is shown in reference 17.

The third turbulence model is the SST model of Menter. (See ref. 22.) This model is based on the observation that in an adverse pressure gradient, the ratio of turbulence shear stress to kinetic energy is nearly constant. Although not applicable to wake reattachment, wall jets, or free turbulent flows, it should give good results in the present application. This model is again a two-layer model composed of equations (6) but with the coefficients for layers 1 and 2 now given by

$$\begin{aligned} \sigma_{k,1} &= 0.85 & \sigma_{\omega,1} &= 0.650 & \beta_1 &= 0.0750 \\ \sigma_{k,2} &= 1.00 & \sigma_{\omega,2} &= 0.856 & \beta_2 &= 0.0828 \end{aligned}$$

The key difference of this SST model with the previous two models is its behavior in an adverse pressure gradient, where the model switches to a shear stress transport model with $\tau = a_1 k$; this is accomplished by defining eddy viscosity by

$$\nu_T = \frac{a_1 k \text{Re}}{\max(a_1 \omega, F_2 \Omega)}$$

with the constant $a_1 = 0.31$ identical to the value used by Menter and Rumsey (ref. 21). The vorticity Ω is given by $\partial u/\partial y$. In the present formulation F_2 equals 1 throughout the boundary layer.

Wilcox in reference 23 shows through an asymptotic analysis of the dissipation rate equation that a balance of the diffusion and dissipation terms in the logarithmic region of an attached turbulent boundary as $y^+ \rightarrow 0$ yields

$$k = 0 \quad \omega = \frac{6\nu}{\beta_1(y^+)^2}$$

This boundary condition is valid for the law of the wall and consistent with viscous sublayer behavior. In a separated turbulent boundary layer, the law of the wall is no longer uniformly correct, although the prevailing condition of a back flow region is one of turbulence interacting independent of mean flow (refs. 24 and 25). The same balance of terms gives the same result with $k \approx (y^+)^{\overline{m}}$ for \overline{m} required to satisfy outer back flow boundary conditions. The same expression is, thus, equally valid for attached and separated turbulent boundary layers. It should also model viscous sublayer behavior without resorting to implementation of a wall function or damping terms. In the present application, a variation of an approximation suggested in reference 26 is used, in which the dissipation rate at the airfoil surface is given by

$$\omega = k_b \frac{60\mu}{\alpha_l \beta_1 (\Delta\eta)^2} \quad (9)$$

for normal mesh spacing $\Delta\eta$ at the base of the boundary layer. Setting $k_b = 1$ simulates the effect of a smooth surface, whereas smaller values simulate increasing roughness.

At the outer edge of the boundary layer ($\eta \rightarrow \infty$), a condition that, at leading order, k and ω remain finite requires that either their first and second derivatives in η tend to zero or that the two parameters be specified. One proposal (ref. 23) is to impose a zero gradient condition at the outer edge by solving the following equations:

$$F_e \frac{d\omega}{d\xi} = -\beta\omega^2$$

$$F_e \frac{dk}{d\xi} = -\beta^*k\omega$$

In this study the values of k and ω are specified upstream and at the outer boundary layer edge. This location makes nonzero turbulence energy and length scale gradients at the outer edge possible but does result in rapid convergence. One solution of these equations, $\omega = F_e[\beta\xi_o(\xi/\xi_o - 1)]^{-1}$ and $k = C_1 F_e^2 \xi_o^{-\beta^*/\beta} (\xi/\xi_o - 1)^{-\beta^*/\beta}$ with $F_e = \text{Constant}$, can be used as an approximation for a more general case with ξ_o as an arbitrary constant of integration from which the initial value $\omega(\xi_a)$ can be set. This solution represents a modeling of the decay of grid-generated turbulence of a flow moving at a uniform speed and therefore is also indirectly dependent on the upstream boundary of the solution domain. In an interacting boundary layer the problem is simplified. We can arbitrarily set $\xi_o = 0$ (i.e., airfoil leading edge ahead of the boundary layer) to ensure consistency of the results to follow for all grids.

In a perturbation analysis of the defect layer equations, Wilcox (ref. 23) has $k \propto u_\tau^2$ and $\omega \propto u_\tau^2/u_e\delta$ in order to return an eddy viscosity proportional to $u_e\delta$. The dissipation and turbulence kinetic energy then are found by

$$\omega = \frac{4|\tau_w/\rho|}{\sqrt{\beta^*}u_e\delta} \quad (10)$$

and k is derived by assuming an algebraic model value of eddy viscosity at the outer boundary layer edge. In equation (10), τ_w and $u_e\delta$ are implemented in a somewhat arbitrary way:

$u_e \delta = 5\alpha_l^{1/2} \text{Re}^{-1/2}$ and $\tau_w = 5\alpha_l^{-1/2} \text{Re}^{-1/2}$. The outer boundary value of kinematic eddy viscosity as used here is given by $\nu_T = (10)^m \nu_{T0}$ ($m = -1, 0, 1$) and $\nu_{T0} = 0.089 u_e \delta \text{Re}^{1/2}$. The parameter m allows varying the free-stream kinematic eddy viscosity and kinetic energy.

Thin-Layer Navier-Stokes Turbulence Model Equations

Two turbulence models are used in the thin-layer Navier-Stokes computations. They are the Menter SST version of the k - ω turbulence model and the SA model. The manner in which the k - ω model is implemented in the thin-layer Navier-Stokes code differs in several ways from the way it is implemented in the interactive boundary layer code. For that reason the k - ω model equations are repeated here. The k - ω SST model equations can be written in the form

$$\left. \begin{aligned} \rho \frac{\partial k}{\partial t} + \rho u_j \frac{\partial k}{\partial x_j} &= P_k \text{Re}^{-1} - \beta^* \rho \omega k \text{Re} + \frac{\partial}{\partial x_j} \left[(\mu + \sigma_{k,n} \mu_T) \frac{\partial k}{\partial x_j} \right] \text{Re}^{-1} \\ \rho \frac{\partial \omega}{\partial t} + \rho u_j \frac{\partial \omega}{\partial x_j} &= P_\omega \text{Re}^{-1} - \beta \rho \omega^2 \text{Re} + 2\rho \sigma_{\omega,2} \frac{1}{\omega} \frac{\partial k}{\partial x_j} \frac{\partial \omega}{\partial x_j} F_1 \text{Re}^{-1} \\ &+ \frac{\partial}{\partial x_j} \left[(\mu + \sigma_{\omega,n} \mu_T) \frac{\partial \omega}{\partial x_j} \right] \text{Re}^{-1} \end{aligned} \right\} \quad (11)$$

The eddy viscosity is given by

$$\mu_T = \min \left(\frac{\rho k}{\omega}, \frac{a_1 \rho k}{\Omega F_2} \text{Re} \right)$$

The production terms are approximated by

$$P_k = \mu_T \Omega^2$$

$$P_\omega = \gamma \rho \Omega^2$$

where Ω is the magnitude of boundary layer vorticity $\partial u / \partial y$. Note that this differs from the production terms used in the interactive boundary layer method where an additional production/destruction term is included. The effect of the difference would be to reduce the turbulence production in a favorable pressure gradient in the interactive boundary layer solution relative to that of the thin-layer Navier-Stokes solution. The constants are calculated from $\phi = (1 - F_1)\phi_1 + F_1\phi_2$, where ϕ_1 and ϕ_2 are the constants given here:

$$\left. \begin{aligned} \sigma_{k,1} &= 0.85 & \sigma_{\omega,1} &= 0.500 & \beta_1 &= 0.0750 \\ \sigma_{k,2} &= 1.00 & \sigma_{\omega,2} &= 0.856 & \beta_2 &= 0.0828 \\ \beta^* &= 0.09 & F_1 &= 1 - \tanh(\Gamma^4) \\ \Gamma &= \min[\max(\Gamma_1, \Gamma_3), \Gamma_2] \\ \Gamma_1 &= \frac{500\nu}{y^2\Omega} \text{Re}^{-2} & \Gamma_2 &= \frac{4\rho\sigma_2 k}{y^2 C D_{k-\omega}} & \Gamma_3 &= \frac{\sqrt{k}}{C_\mu \omega y} \text{Re}^{-1} \\ C D_{k-\omega} &= \max \left(\rho \frac{2\sigma_2}{\omega} \frac{\partial k}{\partial x_j} \frac{\partial \omega}{\partial x_j}, 1 \times 10^{-20} \right) \\ F_2 &= \tanh \Pi & \Pi &= \max(2\Gamma_3, \Gamma_1) \end{aligned} \right\} \quad (12)$$

Note that one of the coefficients and the blending function used in this implementation differ from that used in the interactive boundary layer implementation.

The SA turbulence model equation is

$$\begin{aligned}
\frac{\partial \hat{\nu}}{\partial t} + u_j \frac{\partial \hat{\nu}}{\partial x_j} &= C_{b1}(1 - f_{t2})\Omega \hat{\nu} \\
&+ \left\{ C_{b1}[(1 - f_{t2})f_{\nu 2} + f_{t2}]\kappa^{-2} - C_{w1}f_w \right\} \left(\frac{\hat{\nu}}{d} \right)^2 \text{Re}^{-1} \\
&- \frac{C_{b2}}{\sigma} \hat{\nu} \frac{\partial^2 \hat{\nu}}{\partial x_j^2} \text{Re}^{-1} \\
&+ \frac{1}{\sigma} \frac{\partial}{\partial x_j} \left\{ [\nu + (1 + C_{b2})\hat{\nu}] \frac{\partial \hat{\nu}}{\partial x_j} \right\} \text{Re}^{-1}
\end{aligned} \tag{13}$$

The following definitions are used in this equation:

$$\left. \begin{aligned}
f_{t2} &= C_{t3} \exp(-C_{t4}\chi^2) & f_w &= g \left(\frac{1 + C_{w3}^6}{g^6 + C_{w3}^6} \right)^{1/6} \\
g &= r + C_{w2}(r^6 - r) & r &= \frac{\hat{\nu}}{\hat{S}\kappa^2 d^2 \text{Re}}
\end{aligned} \right\} \tag{14}$$

where

$$\left. \begin{aligned}
\hat{S} &= f_{\nu 3}\Omega + \frac{\hat{\nu}f_{\nu 2}}{\kappa^2 d^2 \text{Re}} & f_{\nu 3} &= \frac{(1 + \chi f_{\nu 1})(1 - f_{\nu 2})}{\chi} \\
f_{\nu 2} &= \frac{1}{(1 + \chi/C_{\nu 2})^3}
\end{aligned} \right\} \tag{15}$$

Eddy viscosity is calculated from the equation

$$\mu_t = \rho \hat{\nu} f_{\nu 1}$$

where

$$f_{\nu 1} = \frac{\chi^3}{\chi^3 + C_{\nu 1}^3} \quad \left(\chi \equiv \frac{\hat{\nu}}{\nu} \right)$$

The constants are

$$\left. \begin{aligned}
C_{b1} &= 0.1355 & \sigma &= 2/3 & C_{b2} &= 0.622 & \kappa &= 0.41 & C_{w2} &= 0.3 \\
C_{w2} &= 2.0 & C_{\nu 1} &= 7.1 & C_{t3} &= 1.2 & C_{t4} &= 0.5 & C_{\nu 2} &= 5.0 \\
C_{w1} &= \frac{C_{b1}}{\kappa} + \frac{1 + C_{b2}}{\sigma}
\end{aligned} \right\} \tag{16}$$

Additional details on the thin-layer Navier-Stokes equations and the numerical method used can be found in reference 2.

Numerical Method for Interactive Boundary Layer Equations

The quasi-simultaneous interactive boundary layer method as implemented by Davis and Werle has been modified for the present application. It couples the unsteady boundary layer

equations solved in finite difference form and the CAP-TSD potential code via a consistent matching condition and interaction law. The TSD solution uses a streamwise flux that approximates an Euler flux to several orders. The turbulence equations are decoupled from the boundary layer equations and solved first at each time step $n + 1$. Mean flow values at the previous time step n are used in the turbulence model computation. The equations are solved with full implicit finite differencing. Both the streamwise and normal derivatives have upwind differencing to enhance diagonal dominance, and the nonlinear coefficients involving k and ω are lagged at the previous time step, giving the turbulence modeling first-order accuracy in time and space.

Mean flow quantities used in the turbulence equations and the values of k and ω actually used in computing eddy viscosity have also been found to result in a more stable boundary layer interaction if smoothing is applied. An averaging function of the form $\Phi = \Sigma\alpha\Phi$ is used with summation over 6 to 9 adjacent grids. In computing equations (6), $\Phi = [F, V]$ is replaced, whereas in computing eddy viscosity, $\Phi = [k, \omega]$ is replaced with averaged values of Φ . Note that in *neither* of these cases is the artificial smoothing applied to either the boundary layer or turbulence field solution directly; thus, the form of the leading order equations (eqs. (6)) being solved is maintained.

For the computation of the finite difference equations, the following terms are defined:

$$\begin{aligned}\tilde{a}_{1i} &= \frac{\alpha_{li}}{\Delta\xi_i} & \tilde{a}_{2i} &= \frac{\alpha_{li}}{\Delta\xi_{i+1}} & \tilde{a}_{3i} &= \frac{\alpha_{li}}{\Delta t} \\ \tilde{b}_i &= \frac{1}{2} + \frac{\alpha_{li}}{2\Delta\xi_i} & \tilde{c}_i &= \frac{\alpha_{li}}{2\Delta\xi_i} \\ \tilde{d}_{1j} &= \frac{1}{\Delta\eta_{j-1}} & \tilde{d}_{2j} &= \frac{1}{\Delta\eta_j} & \tilde{e}_j &= \frac{\Delta\eta_{j-1}}{2\Delta\eta_j\Delta\eta_{ave}} \\ \tilde{f}_j &= \frac{1}{2\Delta\eta_{ave}} \left(\frac{\Delta\eta_j}{\Delta\eta_{j-1}} - \frac{\Delta\eta_{j-1}}{\Delta\eta_j} \right) & \tilde{g}_j &= \frac{\Delta\eta_j}{2\Delta\eta_{j-1}\Delta\eta_{ave}} \\ \tilde{h}_j &= \frac{1}{\Delta\eta_{ave}\Delta\eta_j} & \tilde{i}_j &= \frac{1}{\Delta\eta_{ave}\Delta\eta_{j-1}}\end{aligned}$$

The mesh spacing functions are defined by

$$\Delta\xi_i = \xi_i - \xi_{i-1} \quad \Delta\eta_i = \eta_{i+1} - \eta_i$$

and

$$\Delta\eta_{ave} = \frac{1}{2} (\Delta\eta_j + \Delta\eta_{j-1})$$

The boundary layer equations are finite differenced as follows:

Continuity:

$$\tilde{d}_{1j}(V_{ij}^{n+1} - V_{ij-1}^{n+1}) + \tilde{b}_i(F_{ij}^{n+1} + F_{ij-1}^{n+1}) = \tilde{c}_i(F_{i-1j}^{n+1} + F_{i-1j-1}^{n+1})$$

X-momentum:

$$\begin{aligned}
& L_{ij+1/2} \tilde{h}_j F_{ij+1}^{n+1} - (L_{ij+1/2} \tilde{h}_j + L_{ij-1/2} \tilde{v}_j + \tilde{a}_{3i} - 2\Lambda \tilde{F}^{n+1}) F_{ij}^{n+1} + L_{ij-1/2} \tilde{v}_j F_{ij-1}^{n+1} \\
& + \Lambda F_{ij}^{n+1} (\tilde{e}_j \tilde{V}_{ij+1}^{n+1} + \tilde{f}_j \tilde{V}_{ij}^{n+1} + \tilde{g}_j \tilde{V}_{ij-1}^{n+1}) - V_{ij}^{n+1} [\lambda \tilde{d}_{2j} (\tilde{F}_{ij+1}^{n+1} - \tilde{F}_{ij}^{n+1}) \\
& + (1 - \lambda) \tilde{d}_{1j} (\tilde{F}_{ij}^{n+1} - \tilde{F}_{ij-1}^{n+1})] \\
& + \Lambda \tilde{F}_{ij}^{n+1} (\tilde{e}_j V_{ij+1}^{n+1} + \tilde{f}_j V_{ij}^{n+1} + \tilde{g}_j V_{ij-1}^{n+1}) - \tilde{V}_{ij}^{n+1} [\lambda \tilde{d}_{2j} (F_{ij+1}^{n+1} - F_{ij}^{n+1}) \\
& + (1 - \lambda) \tilde{d}_{1j} (F_{ij}^{n+1} - F_{ij-1}^{n+1})] - \frac{\tilde{a}_{1i} \theta^{n+1}}{\rho_e \theta_e} (p_{ij}^{n+1} - p_{i-1j}^{n+1}) \\
& = \Lambda \tilde{F}_{ij}^{n+1} (\tilde{e}_j \tilde{V}_{ij+1}^{n+1} + \tilde{f}_j \tilde{V}_{ij}^{n+1} + \tilde{g}_j \tilde{V}_{ij-1}^{n+1}) - \tilde{V}_{ij}^{n+1} [\lambda \tilde{d}_{2j} (\tilde{F}_{ij+1}^{n+1} - \tilde{F}_{ij}^{n+1}) \\
& + (1 - \lambda) \tilde{d}_{1j} (\tilde{F}_{ij}^{n+1} - \tilde{F}_{ij-1}^{n+1})] \\
& + \Lambda \tilde{F}^{n+1} \tilde{F}^{n+1} + \tilde{a}_{3i} F_{ij}^n + (1 - \Lambda) \tilde{a}_{2i} (\tilde{F}_{i+1j}^{n+1} - \tilde{F}_{ij}^{n+1})
\end{aligned}$$

Y-momentum:

$$p_{ij+1} - p_{ij} = 0$$

where $L = l + l_T$. In the X-momentum equation (and the turbulence model equations to be shown next)

$$\Lambda = \max \left[\frac{\tilde{F}_{ij}^{n+1}}{|\tilde{F}_{ij}^{n+1}|}, 0 \right]$$

and

$$\lambda = \max \left[\frac{\tilde{V}_{ij}^{n+1}}{|\tilde{V}_{ij}^{n+1}|}, 0 \right]$$

The tilde represents the value from the previous iteration. The matching condition is differenced as follows:

$$\begin{aligned}
& V_{ij \max}^{n+1} - \frac{\eta_{\max}}{\Delta \eta} (V_{ij \max}^{n+1} - V_{ij \max-1}^{n+1}) \\
& = \frac{\sqrt{\alpha l}}{\Delta \xi_i} \left[\rho_e u_e (\delta + \tilde{\theta})_i^{n+1} - \rho_e u_e (\delta + \tilde{\theta})_{i-1}^{n+1} \right]
\end{aligned}$$

The term $\tilde{\theta}$ is explicitly integrated through the boundary layer and is treated as a known quantity at each inversion. The interaction law is of the form

$$u_e^{n+1} = \overline{C}_i + \overline{D}_i \left(\rho_e u_e \delta_i^{n+1} \right)$$

where \overline{C} and \overline{D} result from the inviscid governing equation. Streamwise sweeps of the boundary layer are performed. At the outer edge, the X-momentum equation is replaced with the

interaction law and the Y-momentum equation replaced with the X-momentum equation. The turbulence model equations are differenced as follows:

$$\begin{aligned}
& -L_{\omega_{ij+1/2}} \tilde{h}_j \omega_{ij+1}^{n+1} + (L_{\omega_{ij+1/2}} \tilde{h}_j + L_{\omega_{ij-1/2}} \tilde{i}_j + \tilde{a}_{3i} + \alpha_{li} \beta^* \omega_{ij}^n) \omega_{ij}^{n+1} - L_{\omega_{ij-1/2}} \tilde{i}_j \omega_{ij-1}^{n+1} \\
& + V_{ij}^n [\lambda \tilde{d}_{2j} (\omega_{ij+1}^{n+1} - \omega_{ij}^{n+1}) + (1 - \lambda) \tilde{d}_{1j} (\omega_{ij}^{n+1} - \omega_{ij-1}^{n+1})] \\
& + F_{ij}^n [\Lambda \tilde{a}_{1i} (\omega_{ij+1}^{n+1} - \omega_{i-1j}^{n+1}) + (1 - \Lambda) \tilde{a}_{2i} (\omega_{i+1j}^{n+1} - \omega_{ij}^{n+1})] = \tilde{P}_\omega + \tilde{a}_{3i} \omega_{ij}^n
\end{aligned}$$

and

$$\begin{aligned}
& -L_{k_{ij+1/2}} \tilde{h}_j k_{ij+1}^{n+1} + (L_{k_{ij+1/2}} \tilde{h}_j + L_{k_{ij-1/2}} \tilde{i}_j + \tilde{a}_{3i} + \alpha_{li} \beta \omega_{ij}^n) k_{ij}^{n+1} - L_{k_{ij-1/2}} \tilde{i}_j k_{ij-1}^{n+1} \\
& + V_{ij}^n [\lambda \tilde{d}_{2j} (k_{ij+1}^{n+1} - k_{ij}^{n+1}) + (1 - \lambda) \tilde{d}_{1j} (k_{ij}^{n+1} - k_{ij-1}^{n+1})] \\
& + F_{ij}^n [\Lambda \tilde{a}_{1i} (k_{ij+1}^{n+1} - k_{i-1j}^{n+1}) + (1 - \Lambda) \tilde{a}_{2i} (k_{i+1j}^{n+1} - k_{ij}^{n+1})] = \tilde{P}_k + \tilde{a}_{3i} k_{ij}^n
\end{aligned}$$

where $L_{()} = l + \sigma_{()} n l_T$. The parameters Λ and λ are as defined earlier for the boundary layer equations. These equations are replaced at the outer boundary layer edge with the boundary conditions discussed in a previous section. Solved in this form, the equations decouple resulting in two efficient scalar tridiagonal inversions through the boundary layer.

One or two global subiterations of the turbulence equations at each time step typically are required to reach single precision machine accuracy. The complete code has been vectorized with an average performance on a CRAY Y-MP computer of 41 Mflops, with the inviscid solver requiring approximately 150 Mflops and the boundary layer solver requiring approximately 25 Mflops. Run times for converged steady state solutions are summarized in table 2. They compare quite well with other viscous codes.

Table 2. CPU Execution Times of IBL Code

Grid size	Equivalent C-grid	$\Delta \xi_{\min}$	Δt	Computer time, min (a)
Coarse	134 by 120	0.03	0.015	5
Medium	260 by 120	0.015	0.008	20
Fine	360 by 125	0.008	0.004	55

^aTo converge to within 2 percent of c_l .

Steady Computations

RAE 2822 Airfoil

The accuracy of the interactive boundary layer model is assessed by comparing steady state computations with the data of reference 27 and integral interactive boundary layer and Navier-Stokes results. The $k-\omega$ SST turbulence model is used in both the present interactive boundary layer and thin-layer Navier-Stokes computations. The experimental database for Computer Program Assessment (ref. 27) provides steady pressure, boundary layer, and wake data for several transonic cases. Those to be calculated here are AGARD cases 6, 9, and 10, which range

from the relatively easy case to the fairly difficult case 10 that has quite a strong shock boundary layer interaction. This test also has well-known problems related to tunnel interference, which make corrections to the data necessary. Consequently, a degree of uncertainty exists, especially in case 10.

Experimental transition was fixed at 3 percent chord. In the present computations, transition has been simulated by starting the boundary layer just behind the leading edge with a very small upstream eddy viscosity (or k in the $k-\omega$ model) and placing computational wall surface roughness, through boundary conditions in the turbulence model, from 3 to 5 percent chord.

The first calculated results are for AGARD case 9 shown in figure 1. Except at the upper surface leading edge where the superiority of the Euler solution on a body-fitted coordinate system over the present TSD solution is evident, the present C_p distribution is appreciably better than that of reference 28 using an algebraic turbulence model. The shock strength and location using the present interactive boundary layer method match experiment very well, where algebraic models typically overpredict both shock strength and location. This trend is also evident in the skin friction and displacement thickness distributions presented in figures 2 and 3. The present results in these figures match experiment better except possibly near the leading edge. Otherwise, the recovery aft of the shock is still slightly too strong.

With this case, we can also make a comparison of accuracy and efficiency for grids having differing amounts of grid stretching in the boundary layer. Figure 4 presents c_p distributions for boundary layers having an average of approximately 175 and 85 boundary layer grids normal to the airfoil surface. As shown in table 2, the coarser grid reaches moderate engineering accuracy fairly efficiently. For the sake of accuracy, all the previous and remaining results are with the finer boundary layer grid spacing.

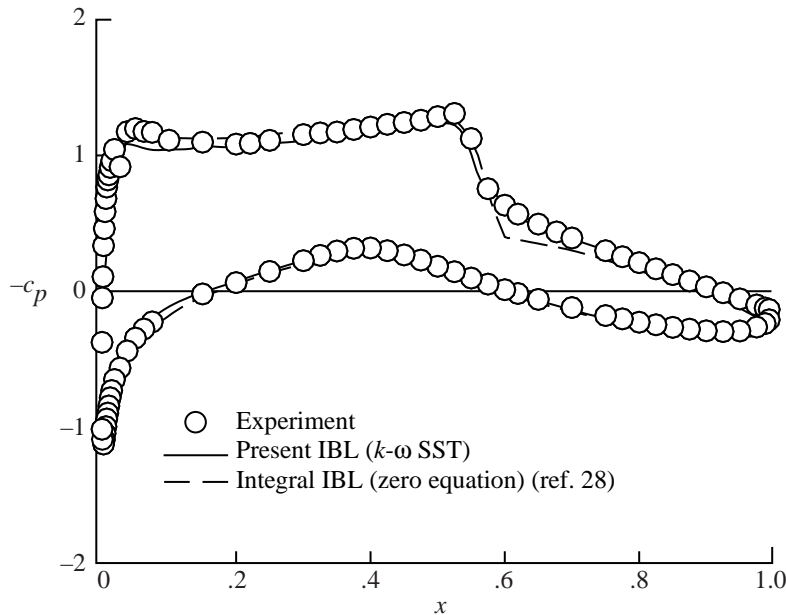


Figure 1. Pressure coefficients for RAE 2822 airfoil, AGARD case 9, at $M_{\text{exp}} = 0.73$, $\alpha = 3.19^\circ$, and $\text{Re} = 6.5 \times 10^6$.

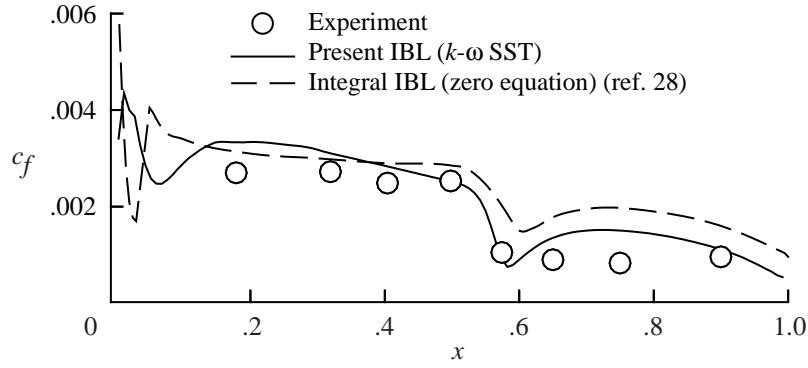


Figure 2. Friction coefficients for RAE 2822 airfoil, A GARD case 9, at $M_{\text{exp}} = 0.73$, $\alpha = 3.19^\circ$, and $\text{Re} = 6.5 \times 10^6$.

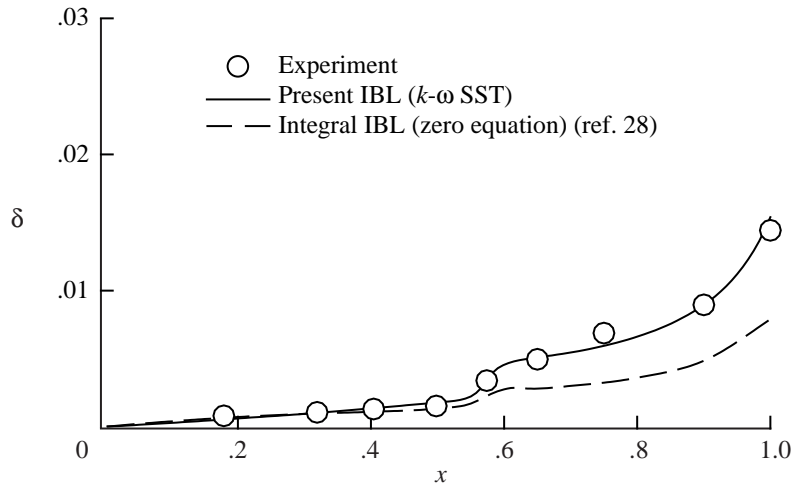


Figure 3. Displacement thicknesses for RAE 2822 airfoil, AGARD case 9, at $M_{\text{exp}} = 0.73$, $\alpha = 3.19^\circ$, and $\text{Re} = 6.5 \times 10^6$.

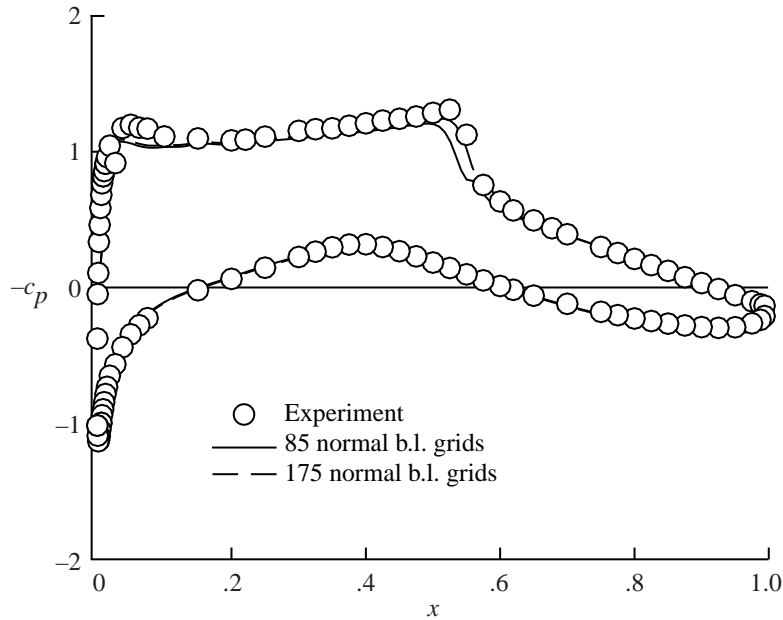


Figure 4. Effect of boundary layer grid stretching for AGARD case 9 at $M_{\text{exp}} = 0.73$, $\alpha = 3.19^\circ$, and $\text{Re} = 6.5 \times 10^6$.

Results using the present interactive boundary layer method are shown with experiment and with other computational results for AGARD case 6. As seen in figure 5, the present results are not quite as good as the very good match of the previous case, although the displacement thickness, seen in figure 6, appears to match experiment well. Since the present method employs a finite differencing of the boundary layer, velocity profiles are also presented in figure 7. Again, except where boundary layer recovery is somewhat too rapid, the results are very good.

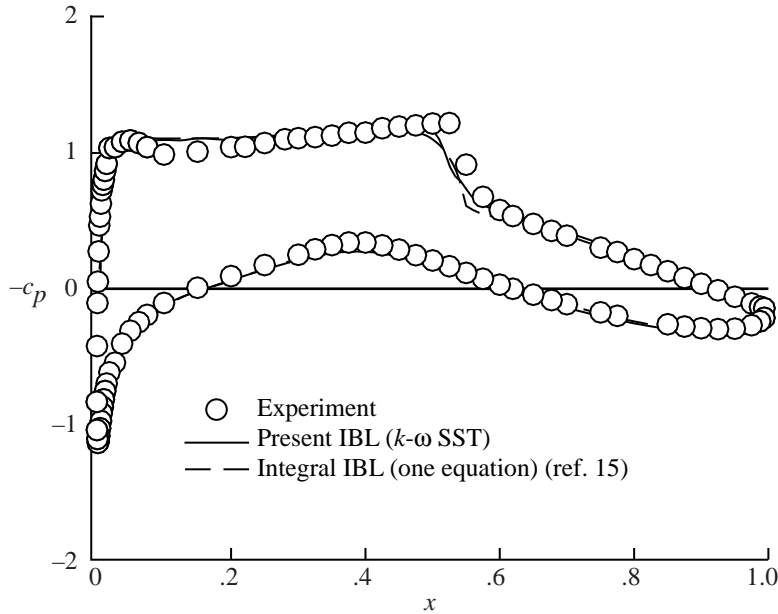


Figure 5. Pressure coefficients for RAE 2822 airfoil, AGARD case 6, at $M_{\text{exp}} = 0.725$, $\alpha = 2.92^\circ$, and $\text{Re} = 6.5 \times 10^6$.

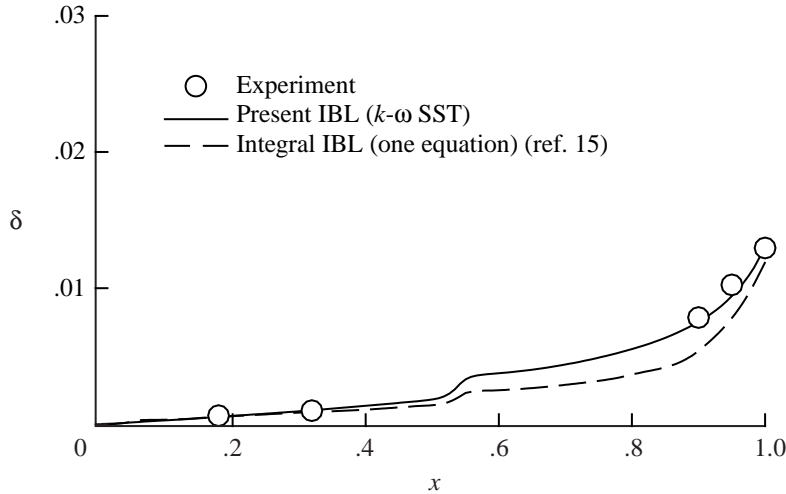


Figure 6. Displacement thicknesses for RAE 2822 airfoil, AGARD case 6, at $M_{\text{exp}} = 0.725$, $\alpha = 2.92^\circ$, and $\text{Re} = 6.5 \times 10^6$.

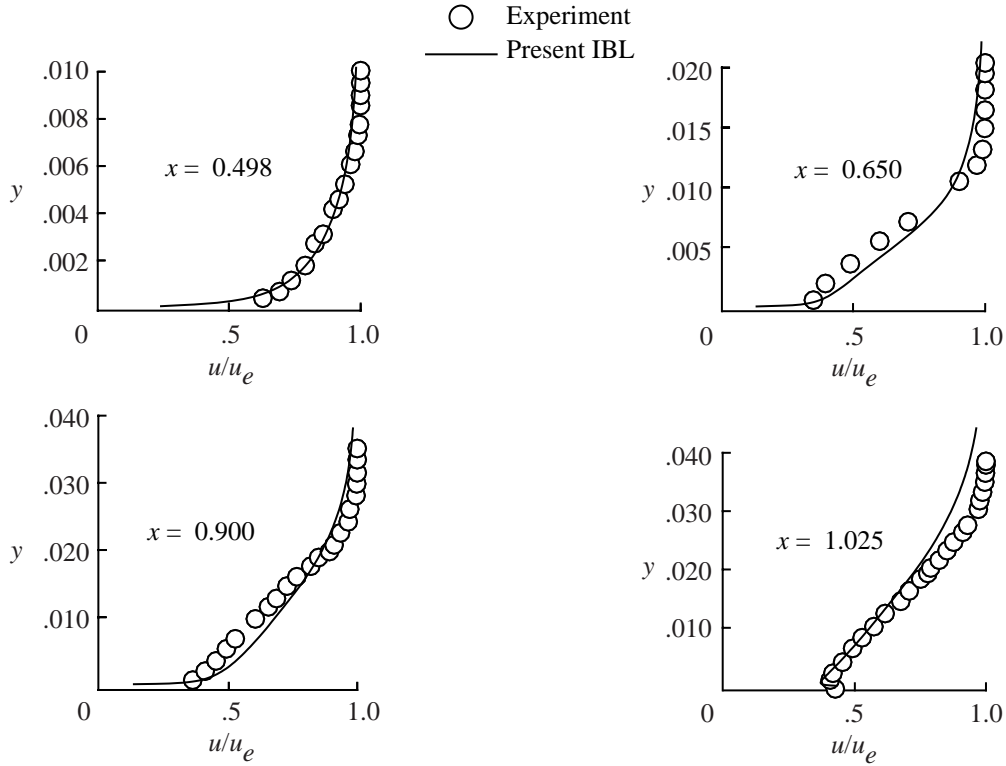


Figure 7. Boundary layer velocity profiles for AGARD case 6 at $M_{\text{exp}} = 0.725$, $\alpha = 2.92^\circ$, and $\text{Re} = 6.5 \times 10^6$.

The conditions so far, with mild viscous-inviscid interaction, have been quite easy. AGARD case 10 is more challenging and takes 3–4 times longer to compute than the previous cases. The integral interactive boundary layer computations of references 15 and 29 are presented in figure 8, and the Navier-Stokes computations of reference 30 using the Johnson-King model are also presented in figure 8. The computations of the other references are at $M = 0.75$ and $\alpha = 2.81^\circ$. With the present method, at $\alpha = 2.81^\circ$, the solution exhibited growing shock oscillations and required a reduction to $\alpha = 2.70^\circ$ to reach a steady state. At this angle, the present results represent a very good match with both experiment and the Navier-Stokes results of reference 30. Finally, note that the accuracy of the present interactive boundary layer computations for all these AGARD cases, which is superior to the integral boundary layer results shown here, may sufficiently justify the present use of a finite differenced boundary layer rather than the empirical and sometimes ad hoc closure relations used in integral boundary layer methods.

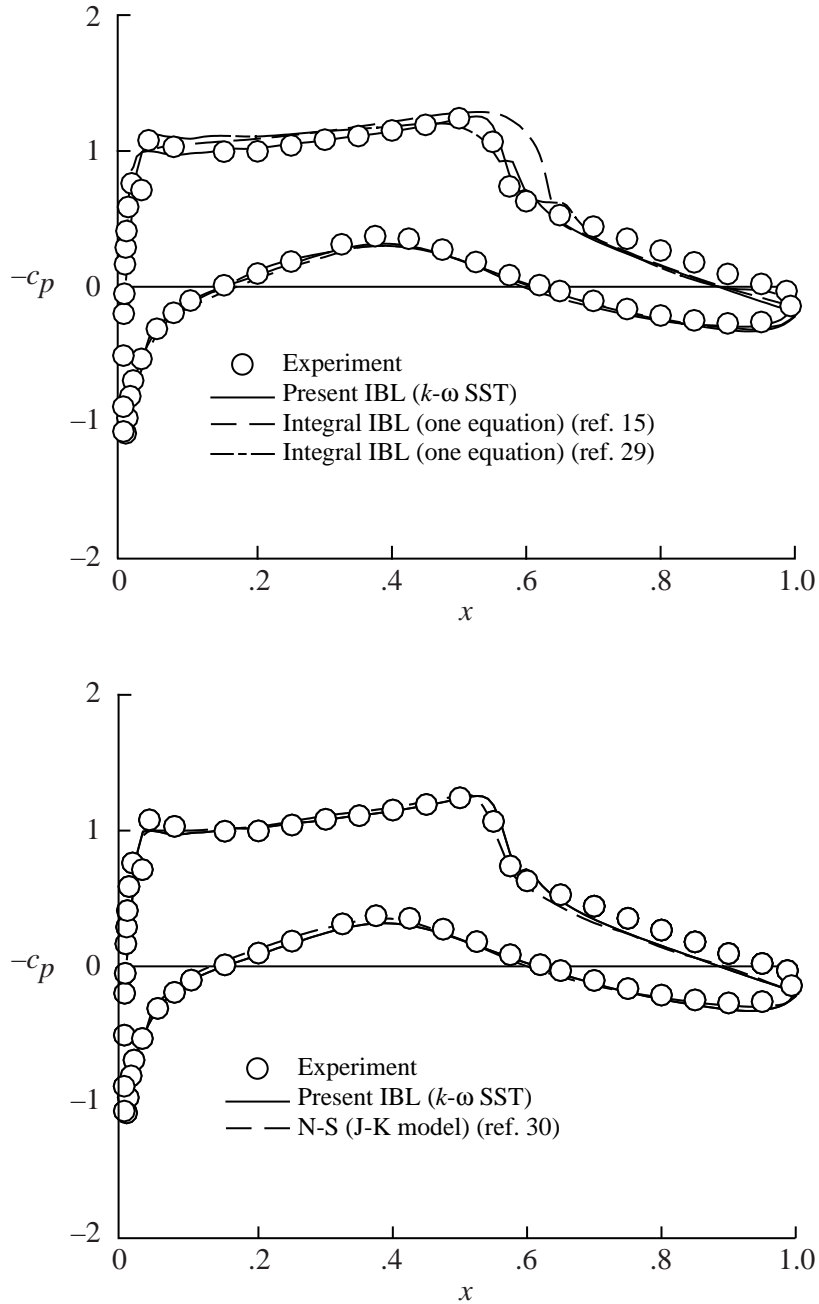


Figure 8. Pressure coefficients for RAE 2822 airfoil, AGARD case 10, at $M_{\text{exp}} = 0.75$ and $\text{Re} = 6.2 \times 10^6$.

NACA 64A010 Airfoil

A steady state solution using the present interactive boundary layer method and the $k-\omega$ SST model has been computed for the NACA 64A010 airfoil at an angle of attack of 2° , $M_\infty = 0.80$, and $\text{Re} = 2 \times 10^6$. At an angle of attack of 2° , the computed flow field separates over approximately 6 percent of the chord, representing a case for which the boundary layer has significant shock separation and yet the available experimental data appear to be steady. Thin layer Navier-Stokes results from using the $k-\omega$ SST turbulence model and experiment, both from reference 21, are presented in figure 9 for comparison with the presently computed interactive boundary layer results. The present SST model results compare quite well with the Navier-Stokes results except near the leading edge and at the shock location.

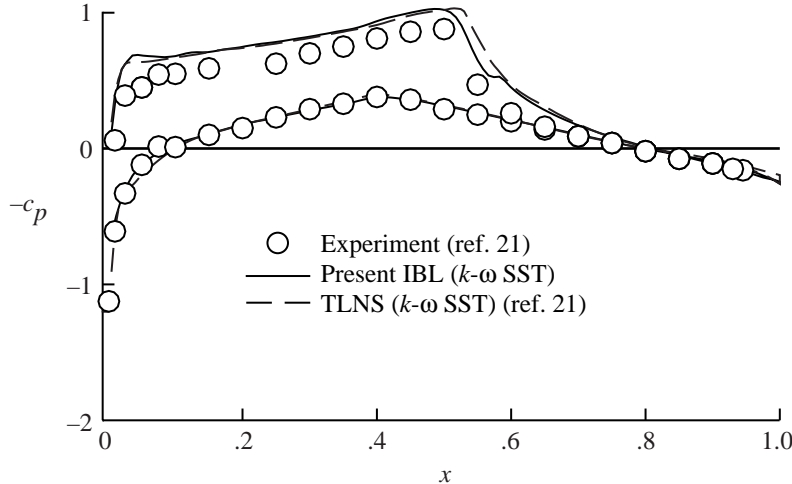


Figure 9. Pressure coefficients for NACA 64A010 airfoil at $M_\infty = 0.80$, $\alpha = 2.0^\circ$, and $Re = 2 \times 10^6$.

NACA 0012 Airfoil

The present interactive boundary layer and thin-layer Navier-Stokes computations both, using the $k-\omega$ SST turbulence model, are presented for a steady condition of reference 8 near shock buffet onset. The thin-layer Navier-Stokes computations use Roe's flux difference splitting with up-wind biased third-order differencing and flux limiter. Multigrid is used to accelerate convergence at each time step. The $k-\omega$ SST turbulence model used in the thin-layer Navier-Stokes computations is identical to that of reference 21. The only structural differences between that and the present interactive boundary layer implementation is the inclusion in the interactive boundary layer model of the production term proportional to kinetic energy, slight differences in the coefficients, and a different blending function.

For the Navier-Stokes computations, several C-grids were tried having various spacings. Each grid gave qualitatively similar results. The grid used in computing the results shown here is moderately fine, with dimensions of 297 by 121. This grid extends 10 chords downstream and 9 chords away from the airfoil. Outer boundary conditions are for free air. Normal wall spacing is $\Delta y^+ \approx 5$. The inner portion of this grid is shown in figure 10. The grid used in the interactive boundary layer computation is the fine grid discussed earlier.

For reference purposes, the thin-layer Navier-Stokes pressure distribution and that from the present interactive boundary layer method are presented in figure 11 for a steady condition just below onset at $M_\infty = 0.775$, $\alpha = 2.05^\circ$, and $Re = 10 \times 10^6$. From 5 to 10 percent chord on the upper surface, aft of the shock, and a portion of the lower surface are the only areas where the two computations differ slightly. Since the authors of reference 2 found that turbulence has a significant impact on buffet computations, an examination of Reynolds stress levels for this steady condition by the two methods is in order. A comparison of the data in figure 12 shows that the interactive boundary layer gives peak values that are less than half those produced by the thin-layer Navier-Stokes implementation up to at least 5 percent chord. The thin-layer Navier-Stokes method on the other hand is producing relatively constant peak turbulence levels from the leading edge with no evidence of transition. The difference in levels at $x = 0.44$ reflects a slight difference in shock location. Otherwise a significantly higher turbulence level is produced by the interactive boundary layer in the outer wake area of the boundary layer combined with a correspondingly thicker boundary layer from the shock to the trailing edge.

This case, just below the experimental shock buffet onset of reference 8, is presented in anticipation of the unsteady computations shown next. Although the thin-layer Navier-Stokes and interactive boundary layer computations of the shock buffet for the supercritical airfoil show good agreement, the shock buffet computations for the NACA 0012 airfoil with the two methods are shown next to give considerably different results.

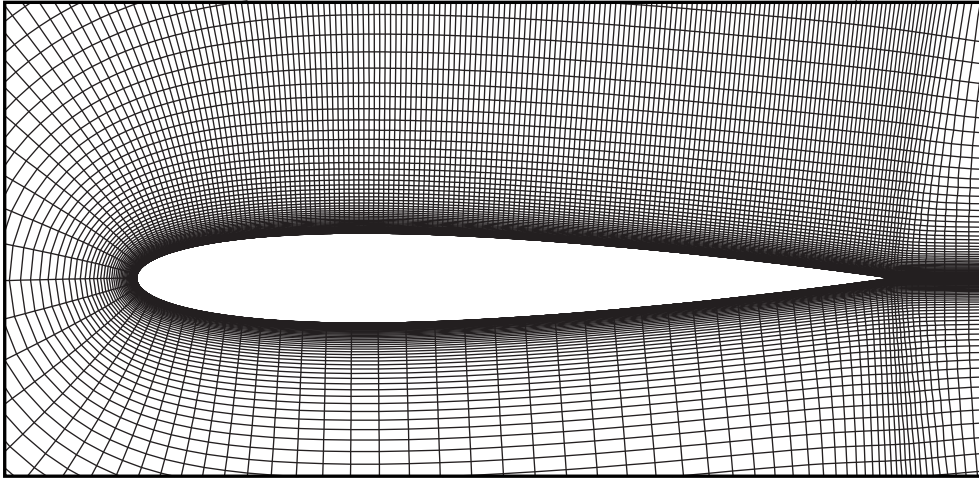


Figure 10. Near field of thin-layer Navier-Stokes grid.

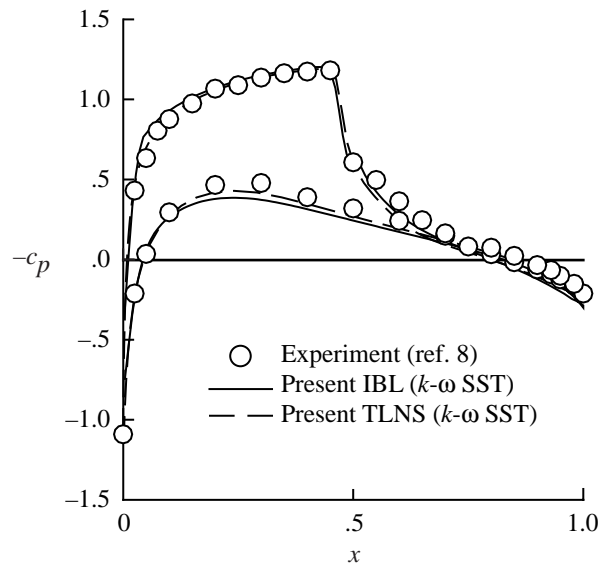


Figure 11. Pressure coefficients for NACA 0012 airfoil at $M_\infty = 0.775$, $\alpha = 2.05^\circ$, and $Re = 10 \times 10^6$.

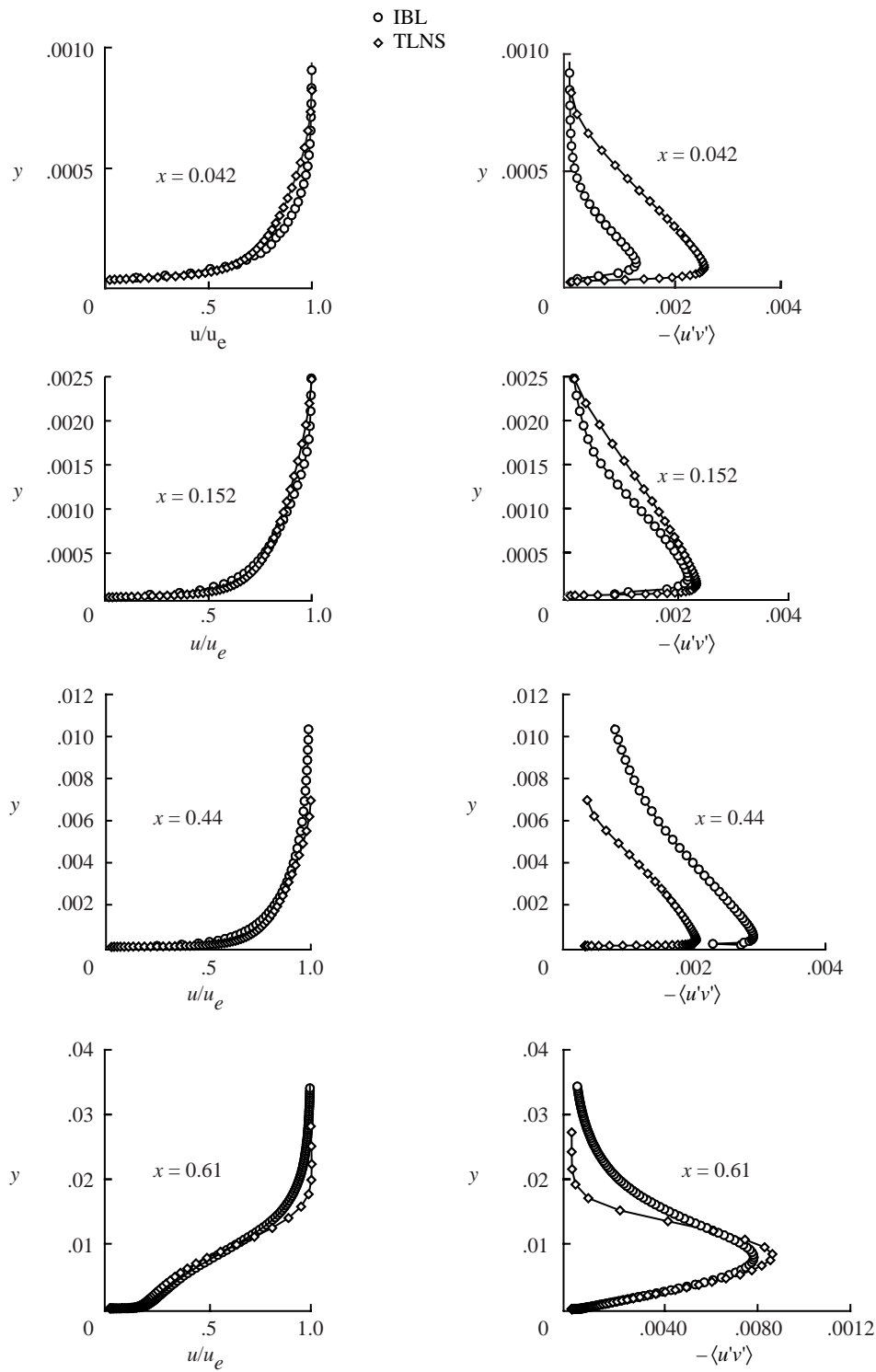


Figure 12. Boundary layer profiles for $k-\omega$ SST model at $M_\infty = 0.775$, $\alpha = 2.05^\circ$, and $\text{Re} = 10 \times 10^6$.

Unsteady Computations

NASA SC(2)-0714 Airfoil

The present interactive boundary layer and thin-layer Navier-Stokes methods have been used to compute in the shock buffet onset region of the NASA SC(2)-0714 airfoil, corresponding to $M_{\text{exp}} = 0.74$ of figure 13. The conditions shown in that figure are from the experimental data set discussed in reference 13 from a high Reynolds number wind tunnel test conducted in the Langley 0.3-Meter Transonic Cryogenic Tunnel. The purpose of this test was to provide data of transonic conditions of a fixed and pitching NASA SC(2)-0714 airfoil through a range of Reynolds numbers. Reference 13 documents cases for fixed angles of attack from that test, some of which show shock buffet. These data are significant in the present context not only because shock buffet is displayed but because a slight Reynolds scaling is revealed in the onset location. The data require, however, significant correction for wind tunnel effects such as downwash or Mach number. For instance, based on the theory of reference 31, at $c_l = 0.93$, the angle of attack corrected to account for induced downwash would be $\Delta\alpha = -1.6^\circ$. The corrected Mach numbers for this wind tunnel are found in reference 32. Only the Mach number corrections are used in the computations to follow.

The experimental conditions showing shock buffet are cases 5 and 7 in figure 13 which are at $M_{\text{exp}} = 0.74$, $\alpha = 3.0^\circ$, and $\text{Re} = 15 \times 10^6$ and 30×10^6 , respectively. Those experimental data display a Reynolds scaling effect in the location of the shock buffet onset, a feature that is also shown in the present computations. In the computations that follow, the critical point at which onset occurred was found by increasing the angle of attack by increments of 0.2° until onset occurs and interpolating to the bifurcation point. The bifurcation point location was inferred by the relative decay or growth rates of the shock oscillation at successive angles of attack. To assess the sensitivity of these computations to the grid used, this procedure was repeated with the three grids discussed previously. The buffet boundary was identical for all to within $\pm 0.1^\circ$. Based on this result, the shock buffet interactive boundary layer computations were made with the finest of the three interactive boundary layer grids.

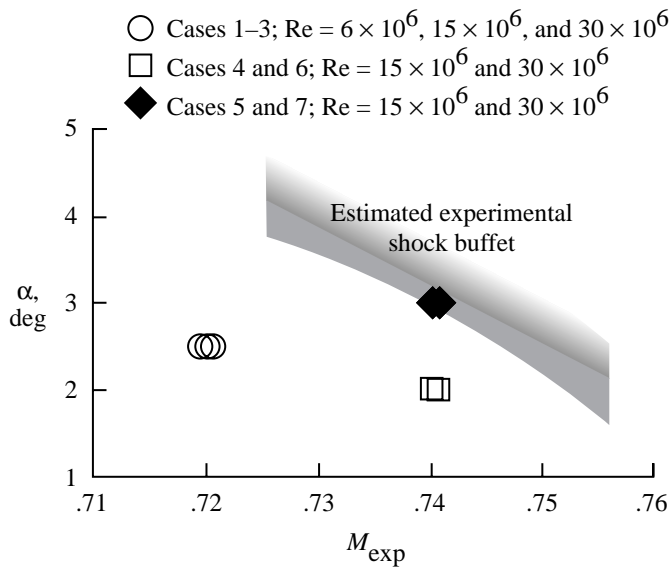


Figure 13. Experimental data (ref. 13) for NASA SC(2)-0714 airfoil, steady and unsteady cases.

Interactive boundary layer results shown in the figures discussed subsequently are compared with experimental data from reference 13. As seen in figure 14, computed onset is very near the angle of attack of the experimental shock buffet at $\alpha = 3.0^\circ$, but the solution reveals a slight Reynolds number effect. This effect is made clearer by the unsteady pressure coefficient moduli plotted in figure 15 for solutions at successive angles of attack. Quite near buffet onset, a difference in intensity at different Reynolds numbers exists whereas deeper into buffet, difference diminishes. The similarity of the solutions near buffet onset with the data shown in figure 16 suggests that the experimental conditions are also very near shock buffet onset. Figure 17 presents computed and experimental upper surface mean pressure coefficient distributions for cases 5 and 7. The computed mean c_p chordwise distributions in figure 17 and the normalized unsteady $|\hat{c}_p|$ distributions in figure 15 suggest that the angle of attack to match the experiment at $\alpha_{\text{exp}} = 3.0^\circ$ should be computed at an angle of attack close to that angle. On the other hand, figure 18 shows the computed frequency approaching experiment slightly as the angle of attack is increased to 3.4° . This feature and the fact that the corrected angle of attack based on reference 31 would be $\alpha_{\text{corr}} = 1.4^\circ$ is somewhat puzzling. The experimentally observed rearward shift of the shock oscillations with increasing Reynolds number is also not represented in the numerical solutions. The computations place the region of shock oscillation several percent forward at the higher Reynolds number.

Thin-layer Navier-Stokes computations with the SA model are shown next, for conditions near the shock buffet case 5 of figure 13 at a Reynolds number of 15×10^6 . The grid used had mesh spacing essentially the same as that used in the steady NACA 0012 thin-layer Navier-Stokes computations discussed earlier. Wall spacing is $\Delta y^+ \approx 6$. To initiate the thin-layer Navier-Stokes computations, a steady solution at an angle of attack several degrees below experimental buffet onset was obtained. Second-order time accurate computations were begun with step jumps

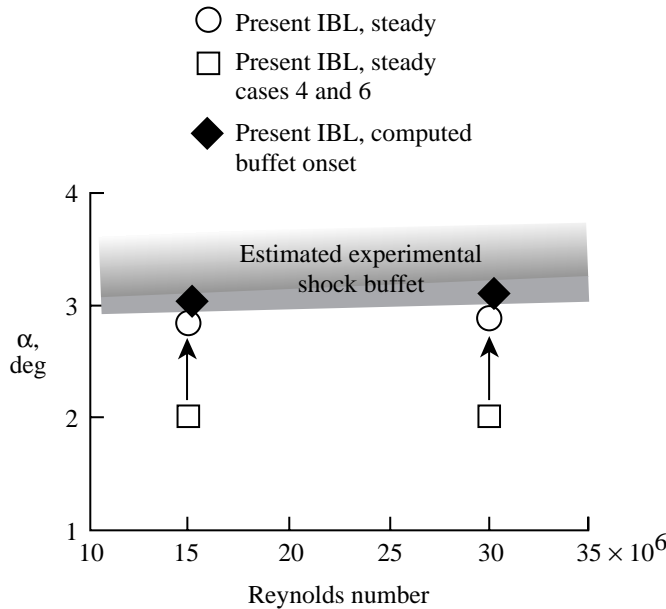


Figure 14. Computed shock buffet onset for NASA SC(2)-0714 airfoil, $k-\omega$ SST model, at $M_{\text{comp}} = 0.725$ and $M_{\text{exp}} = 0.74$.

in the angle of attack with an amplitude of $\pm 2^\circ$ to approximate a single shock oscillation; this was used to initiate the shock buffet. A time step size of 0.04 (nondimensionalized by speed of sound) was used for the time accurate computations with 4–5 subiterations per time step and multigrid. The computations were continued to either a steady state or a converged limit cycle oscillation.

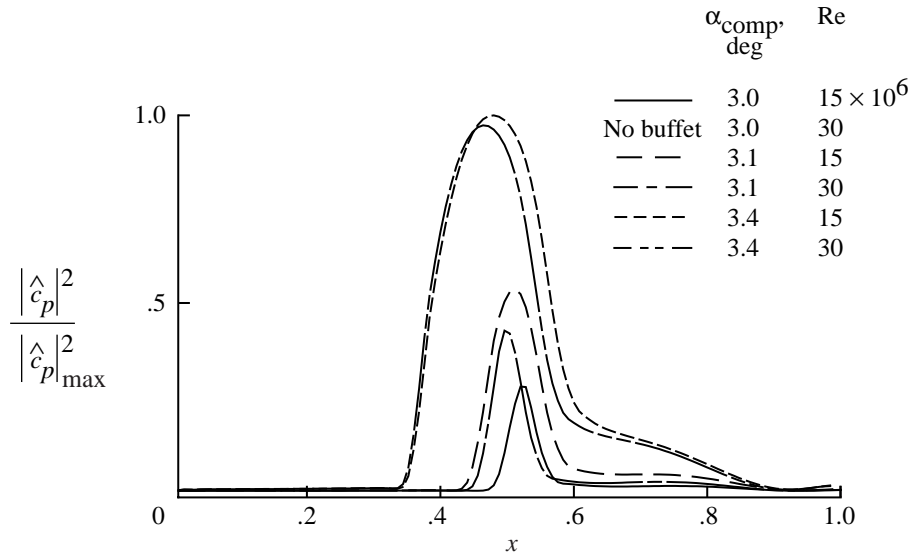


Figure 15. Shock buffeting normalized moduli for NASA SC(2)-0714 airfoil at $M_{\text{comp}} = 0.725$ on upper surface. Present IBL.

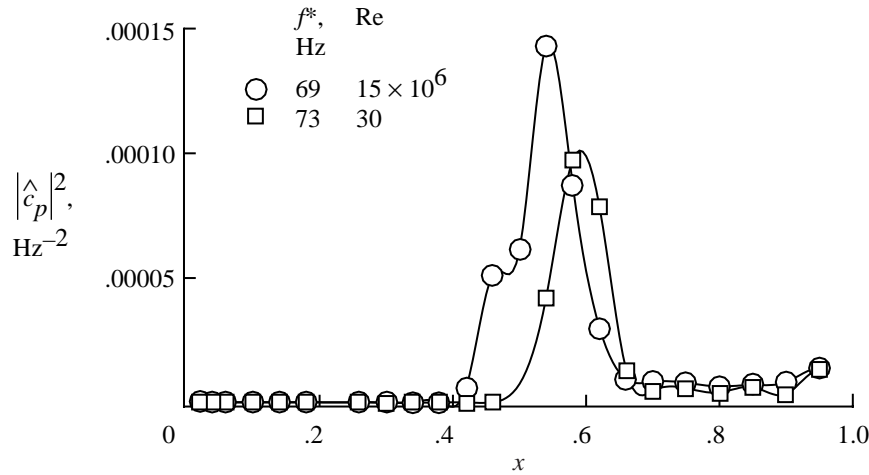


Figure 16. Shock buffet moduli for NASA SC(2)-0714 airfoil at peak frequencies for cases 5 and 7 at $M_{\text{exp}} = 0.74$ and $\alpha_{\text{exp}} = 3.0^\circ$ on upper surface. Experimental data from reference 13.

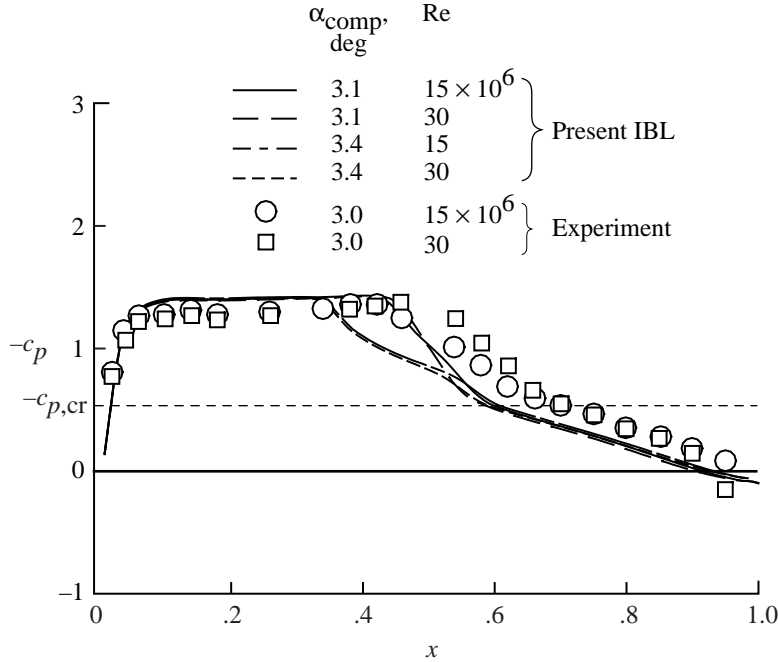


Figure 17. Shock buffet mean pressure coefficients for NASA SC(2)-0714 airfoil at $M_{comp} = 0.725$ on upper surface.

This procedure was repeated at successive angles of attack at increments of $1/2^\circ$. The results of these computations are shown in figures 18 to 22. These results compare reasonably well with experiment as well as with the IBL computations. Onset of shock buffet occurs between the angles of attack from 3° to 3.5° ; this is compared with an onset at an angle of attack of 2.97° from the IBL computation. The c_l trace of figure 20 shows shock oscillations at $\alpha = 3.5^\circ$ having reached converged limit cycle behavior, the frequency of which is quite close to that of experiment. (See fig. 18.) The interactive boundary layer and thin-layer Navier-Stokes mean c_p distributions in figure 21 are in moderate agreement, although the thin-layer Navier-Stokes computation is in somewhat better agreement with experiment in the shock region. The pressure recovery toward the trailing edge is also somewhat more rapid in the interactive boundary layer solution. Figure 22 shows experimental chordwise distributions of $|\hat{c}_p|$ normalized to peak values of the fundamental along with those of the interactive boundary layer and thin-layer Navier-Stokes computations. The relative magnitudes of the computed fundamental and first harmonic match experiment very well, although in both the chordwise extent of the shock oscillation is forward of experiment. Both underestimate the overall extent as well. For example, the shock motion extent in the thin-layer Navier-Stokes computation is roughly half that of the experiment.

This comparison of both computed results with experiment offers hope that both the interactive boundary layer and the thin-layer Navier-Stokes methods give a reasonably accurate computation of shock buffet onset. As seen in the next section this view may be premature.

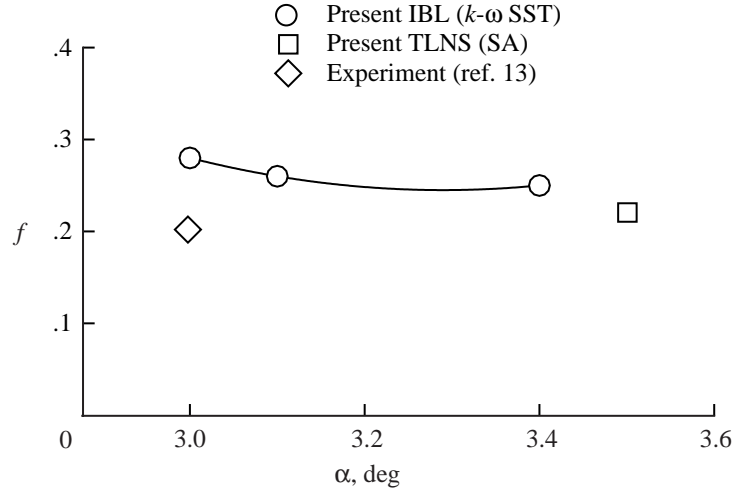


Figure 18. Shock buffet frequencies for NASA SC(2)-0714 airfoil for case 5.

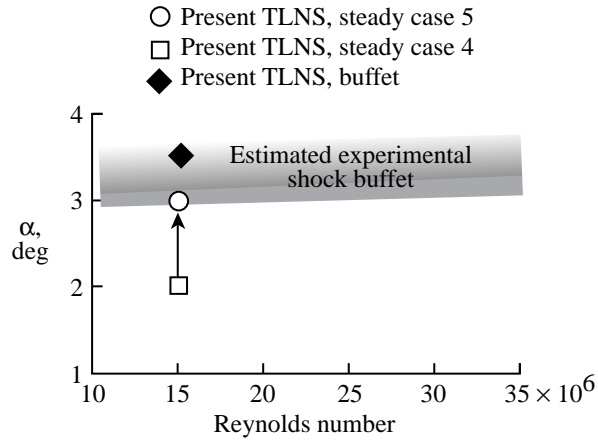


Figure 19. Computed shock buffet onset for NASA SC(2)-0714 airfoil, SA model, at $M_{\text{comp}} = 0.725$ and $M_{\text{exp}} = 0.74$.

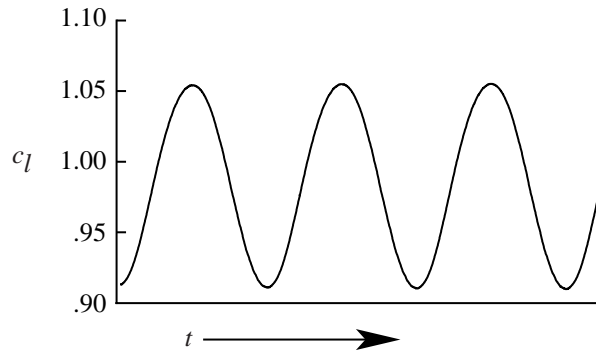


Figure 20. Shock buffet lift coefficients for NASA SC(2)-0714 airfoil, SA model, at $M_{\text{comp}} = 0.725$, $\alpha_{\text{comp}} = 3.50^\circ$, and $Re = 15 \times 10^6$. Present TLNS.

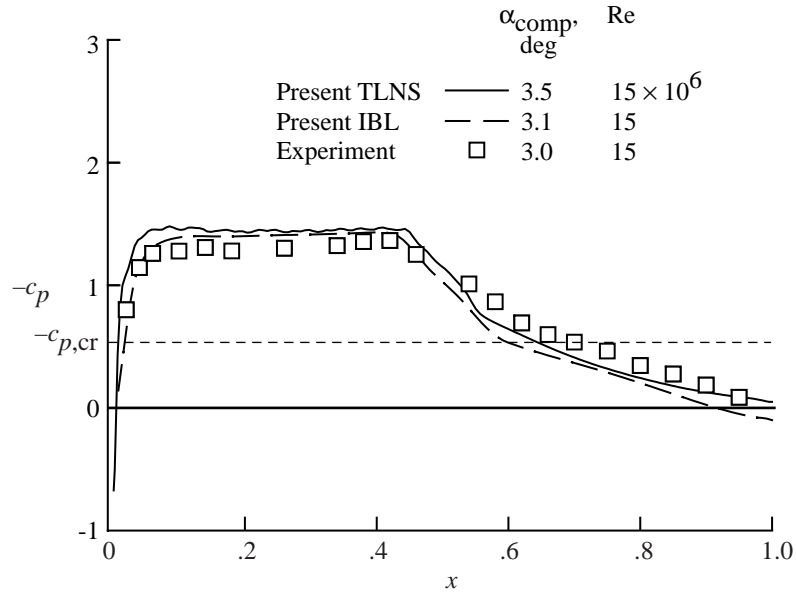


Figure 21. Shock buffet mean pressure coefficients for NASA SC(2)-0714 airfoil at $M_{\text{comp}} = 0.725$ on upper surface.

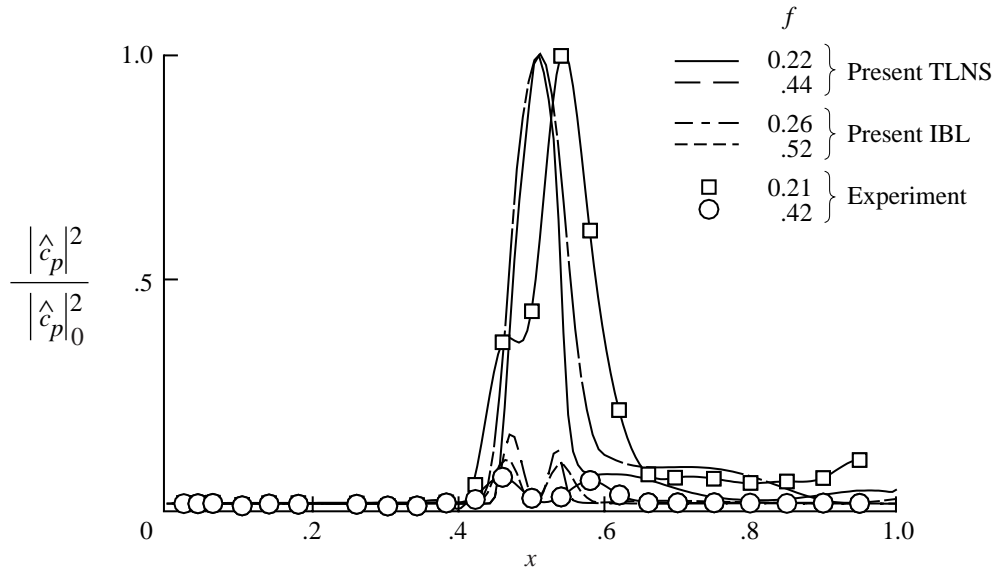


Figure 22. Shock buffet normalized moduli for NASA SC(2)-0714 airfoil, fundamental and harmonic, case 5, at $M_{\text{comp}} = 0.725$ and $\alpha_{\text{comp}} = 3.10^\circ$ (IBL) and 3.5° (TLNS) on upper surface.

NACA 0012 Airfoil

The present interactive boundary layer and thin-layer Navier-Stokes methods have been used to compute in the shock buffet onset region of the NACA 0012 airfoil. In view of the sensitivity of shock buffet to turbulence modeling observed in other studies and the extensive data available for this airfoil, an analysis has been made of the effect of turbulence model parameters on buffet onset with the interactive boundary layer model. For the interactive boundary layer computations, the medium resolution grid was used in comparisons of turbulence models to reduce computation times. The time step was 0.012 with 2 to 3 boundary layer subiterations per time step. In assessing onset location for each of the turbulence models, the angle of attack was successively increased by increments of 0.2° . Onset was taken as the first angle at which computed oscillations continued to grow after several initial cycles of transient shock oscillations had passed.

The buffet boundaries found by using the present interactive boundary layer method and other published results along with the experimental values from reference 8 are shown in figure 23. The $k-\omega$ SST turbulence model uniformly gives the boundary lower than the other turbulence models and overall represents the best match of all the models. Both the Wilcox one and two layer models appear to give only slight improvement over results with an algebraic model. From figure 24, there is also a rather modest decrease in onset angle with decrease in the value of turbulence kinetic energy k at the boundary layer edge corresponding to a lower free-stream turbulence level.

The thin-layer Navier-Stokes shock buffet onset computations for this airfoil were done with both the $k-\omega$ SST and the SA turbulence models. The same procedure was used for these computations as for the supercritical airfoil. To initialize, a steady state solution was obtained at an angle of attack of 2° below experimental buffet onset. A steady lift coefficient was obtained. Second-order time accurate computations were begun by using time steps of 0.005 and 0.04 with the $k-\omega$ SST and SA turbulence models, respectively. Step jumps in the angle of attack with an amplitude of $\pm 2^\circ$ simulating a single shock oscillation were used to start the shock buffet.

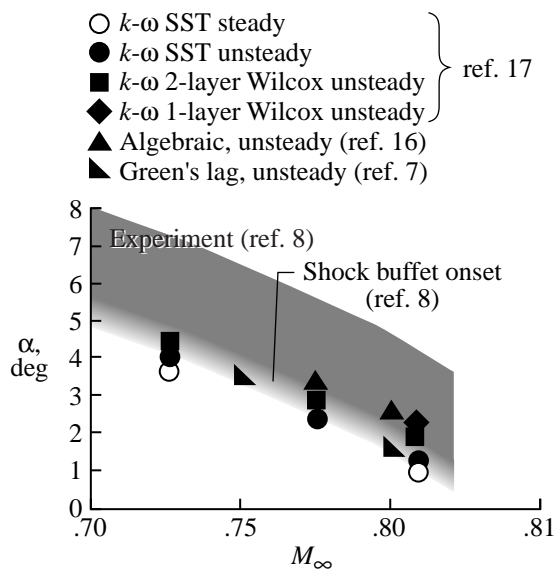


Figure 23. Computed shock buffet onset found by various turbulence models and experiment for NACA 0012 airfoil. IBL.

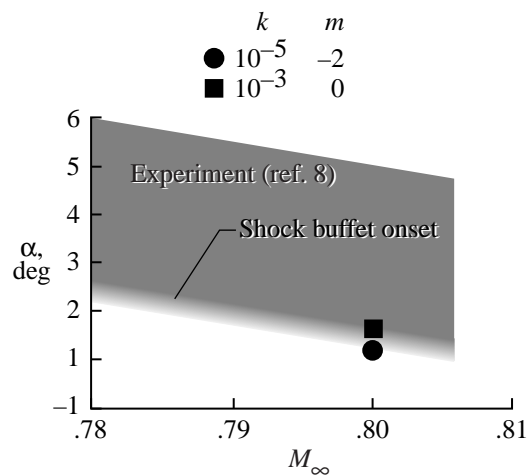


Figure 24. Effect of boundary layer edge turbulence kinetic energy on shock buffet onset. Present IBL.

Computations were completed with the two turbulence models at the highest Mach number at a final angle of attack well into the buffet region. Because of a time step restriction, apparently imposed by the $k-\omega$ SST model, this is the only unsteady computation that has been made by using that model. Although comparison of the SA and the $k-\omega$ SST model results are not shown, computation confirmed that the two models give very similar results in the shock buffet region and that the ensuing thin-layer Navier-Stokes computations could be concluded with the SA model alone. Accordingly, all unsteady results shown have been computed with the SA model.

The results of this investigation are shown in figures 25 and 26. At $M_\infty = 0.775$ and $\alpha = 4.0^\circ$, the c_l oscillation amplitude had damped to about 10 percent of the peak excursion 1 1/2 cycles after the driving force was eliminated. (See fig. 26(a).) Computations several cycles farther showed oscillations continuing to damp out. Although skin friction is not shown, the final steady state solution has a significant shock separation that marginally reattaches just before the trailing edge. This procedure was repeated at higher angles of attack with a similar level of damping. Computations at $M_\infty = 0.75$ over a range of angle of attack give slightly less damped shock oscillations, whereas at a Mach number of 0.725 the shock oscillations are even less damped. These results have been obtained with the turbulence model computed throughout the flow field. The effect of a turbulent transition occurring in the 10-percent-chord range has been simulated as well by turning the turbulence production terms on at 10 percent chord with zero turbulence production ahead of that point. This effectively creates a laminar flow in the leading edge region. As seen in figure 26(b), computing the turbulence from the leading edge and starting at 10 percent chord appeared to have little effect on the outcome. A variation in the level of damping is also seen at the lower Mach number. At $\alpha = 6^\circ$, just beyond onset, the oscillations die out slowly, whereas at $\alpha = 9^\circ$ the oscillations are again strongly damped. (Compare fig. 26(b) with fig. 26(c).) It is interesting to note a variation in amplitude in the limit cycle shock buffet with angle of attack in the interactive boundary layer computations of reference 7 for this airfoil.

In summary, thin-layer Navier-Stokes computations with the NASA SC(2)-0714 airfoil have shown sustained shock buffet that compares well with experiment. The present thin-layer Navier-Stokes computations with the NACA 0012 airfoil have shown moderate to strongly damped shock

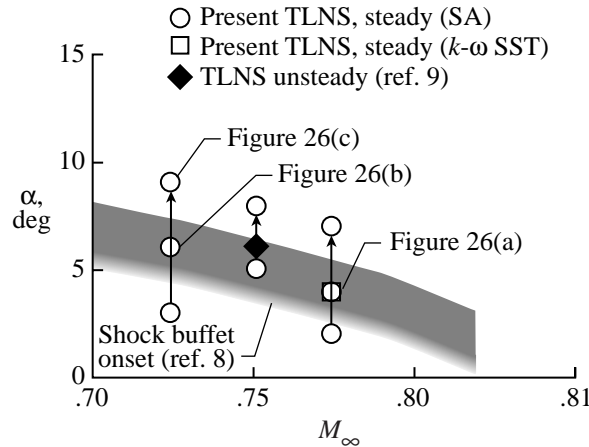
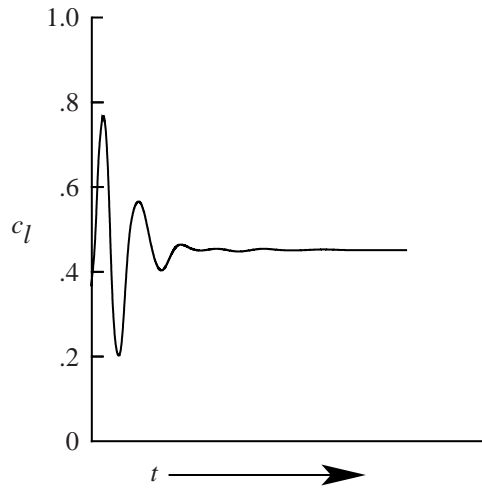
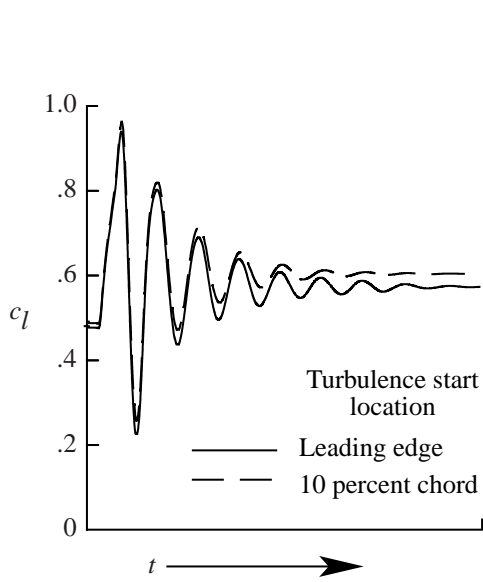


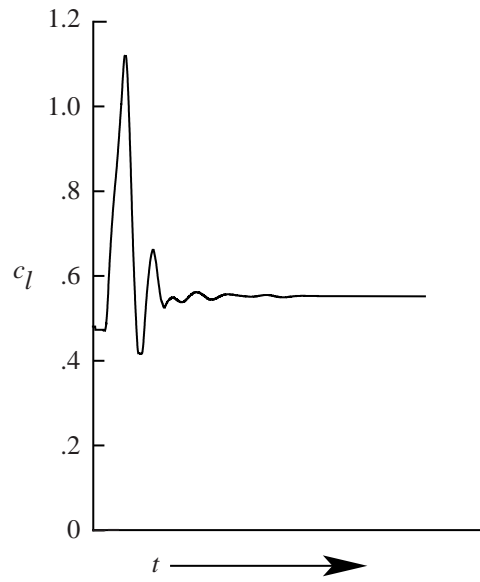
Figure 25. Shock buffet onset for NACA 0012 airfoil.



(a) $\alpha = 4^\circ$; $M_{\text{comp}} = 0.775$.



(b) $\alpha = 6^\circ$; $M_{\text{comp}} = 0.725$.



(c) $\alpha = 9^\circ$; $M_{\text{comp}} = 0.725$.

Figure 26. Computed lift coefficients for NACA 0012 airfoil at $\text{Re} = 10 \times 10^6$.

oscillation, with no evidence of a developing limit cycle shock buffet. Turbulence transition location does not significantly alter this situation for the NACA 0012 airfoil. A limited effort at refinement of the TLNS grid likewise has not resulted in sustained shock oscillations. As for differences in the solutions of the two airfoils, clearly the supercritical airfoil has a stronger viscous-inviscid interaction behind the shock than does the conventional airfoil; this can be seen in the comparison of the skin friction for the two airfoils shown in figure 27. This and the fact that differences in the amount of trailing edge separation due to Reynolds scaling effects result in somewhat different onset locations at different Reynolds numbers for the NASA SC(2)-0714 airfoil tend to confirm that trailing edge interaction has a considerable effect on the onset of shock buffet. Geometry certainly plays a role, the effect of which has not been fully explored in this report.

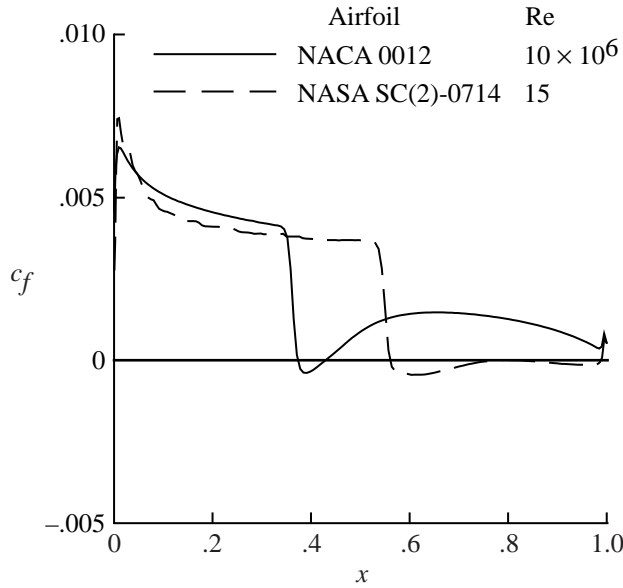


Figure 27. Skin friction coefficients for two airfoils at $M_\infty = 0.725$ and $\alpha = 3.0^\circ$. Present TLNS.

Concluding Remarks

An interactive boundary layer method using a transonic small disturbance, potential outer flow model with an Euler-like streamwise flux has been coupled with several variations of the $k-\omega$ turbulence model. This method has been found to compute very accurately many standard steady transonic test cases. Several steady computations have shown that the interactive boundary layer method is capable of giving results that compare very well with thin-layer Navier-Stokes results. Turbulence levels differed in some minor respects between the two methods, but in general, these results confirm that the interactive boundary layer method is capable of quite good accuracy. This accuracy, which is superior to many other integral boundary layer results, is also justification for the use of a finite differenced boundary layer, showing the boundary layer method at its best, rather than resorting to the more widely used empirical and sometimes ad hoc closure relations used in integral boundary layer methods.

With the interactive boundary layer method, a study has been made of the flow and turbulence modeling necessary to accurately model shock buffet onset. Both the interactive boundary layer and a thin-layer Navier-Stokes method have been employed. Computations using the two methods in the shock buffet region of a 14-percent-thick supercritical airfoil compare well with experiment. These results suggest that both methods are capable of modeling shock buffet onset of that airfoil quite well.

Variants of the $k-\omega$ turbulence model with the interactive boundary layer method have been used to compute shock buffet onset for the NACA 0012 airfoil. These solutions confirm that turbulence model has an influence on the accuracy of the computed onset location most notably at higher Mach numbers. When comparing the interactive boundary layer and thin-layer Navier-Stokes computations, the results from the two methods were found to be quite different when computing the shock buffet of the NACA 0012 airfoil. The shock buffet onset computed with the interactive boundary layer and the $k-\omega$ SST (shear stress transport) turbulence model compares well with the onset of shock buffet seen in the data of NASA TP-2485. In contrast, the present thin-layer Navier-Stokes computations have uniformly shown damped shock oscillations well into the shock buffet region. Transition locations fixed respectively at the leading edge and at 10 percent chord were found to yield qualitatively similar thin-layer Navier-Stokes results.

From the computed results, the supercritical airfoil has a much stronger viscous-inviscid interaction behind the shock than the conventional airfoil. Trailing-edge viscous-inviscid interaction has been shown by these results to have a considerable effect on the onset of shock buffet. What remains to be assessed computationally is the influence of wind tunnel walls and the effect of the numerical accuracy of the thin-layer Navier-Stokes scheme used in this report.

NASA Langley Research Center
Hampton, VA 23681-2199
October 8, 1997

References

1. Gillan, Mark A.: Navier-Stokes Simulation of Self-Excited Shock Induced Oscillations. AIAA-95-1809, June 1995.
2. Rumsey, Christopher L.; Sanetrick, Mark D.; Biedron, Robert T.; Melson, N. Duane; and Parlette, Edward B.: Efficiency and Accuracy of Time-Accurate Turbulent Navier-Stokes Computations. *Proceedings of the 13th AIAA Applied Aerodynamics Conference*, June 1995, pp. 1–15. (Available as AIAA-95-1835.)
3. Mabey, D. G.; Welsh, B. L.; and Cripps, B. E.: *Periodic Flows on a Rigid 14% Thick Biconvex Wing at Transonic Speeds*. RAE-TR-81059, British R.A.E., May 1981.
4. McDevitt, John B.; Levy, Lionel L., Jr.; and Deiwert, George S.: Transonic Flow About a Thick Circular-Arc Airfoil. *AIAA J.*, vol. 14, no. 5, May 1976, pp. 606–613.
5. Stanewsky, E.: Shock Boundary Layer Interaction. *Boundary Layer Simulation and Control in Wind Tunnels*, AGARD-AR-224, Apr. 1988, pp. 271–305.
6. Redeker, G.: Calculation of Buffet Onset for Supercritical Airfoils. *Proceedings Transonicum II Symposium*, Springer-Verlag, 1976, pp. 66–74.
7. Edwards, John W.: Transonic Shock Oscillations Calculated With a New Interactive Boundary Layer Coupling Method. AIAA-93-0777, Jan. 1993.
8. McDevitt, John B.; and Okuno, Arthur F.: *Static and Dynamic Pressure Measurements on a NACA 0012 Airfoil in the Ames High Reynolds Number Facility*. NASA TP-2485, 1985.
9. Hirose, Naoki; and Miwa, Hitoshi: *Computational and Experimental Research on Buffet Phenomena of Transonic Airfoils*. NAL-TR-996T, Sept. 1988.
10. Harris, C. D.: *Two-Dimensional Aerodynamic Characteristics of the NACA 0012 Airfoil in the Langley 8 Foot Transonic Pressure Tunnel*. NASA TM-81927, 1981.
11. Roos, Frederick W.: Some Features of the Unsteady Pressure Field in Transonic Airfoil Buffeting. *J. Aircr.*, vol. 17, no. 11, Nov. 1980, pp. 781–788.
12. Roos, F. W.: Surface Pressure and Wake Flow Fluctuations in a Supercritical Airfoil Flowfield. AIAA-75-66, Jan. 1975.
13. Bartels, Robert E; and Edwards, John W.: *Cryogenic Tunnel Pressure Measurements on a Supercritical Airfoil for Several Shock Buffet Conditions*. NASA TM-110272, 1997.
14. Kandula, M.; and Wilcox, D. C.: An Examination of $k-\omega$ Turbulence Model for Boundary Layers, Free Shear Layers and Separated Flows. AIAA-95-2317, June 1995.
15. Velichko, S. A.; and Lifshitz, Yu. B.: Numerical Simulation of Viscous Transonic Flows Over an Airfoil. *Theor. & Comput. Fluid Dyn.*, vol. 7, 1995, pp. 189–206.
16. Girodroux-Lavigne, P.; and Le Balleur, J. C.: *Time-Consistent Computation of Transonic Buffet Over Airfoils*. ONERA TP-1988-97, 1988.
17. Bartels, Robert E.: Interactive Boundary Layer Computations Using the Improved $k-\omega$ Turbulence Model. *Numerical Methods in Laminar and Turbulent Flow*, Volume 9, Part 1, C. Taylor and P. Durbetaki, eds., Pineridge Press, 1995, pp. 561–572.
18. Batina, John T.: Unsteady Transonic Small-Disturbance Theory Including Entropy and Vorticity Effects. *J. Aircr.*, vol. 26, June 1989, pp. 531–538.
19. Deiwert, George S.: Finite Difference Simulation of Unsteady Interactive Flows. *Computational Methods in Viscous Flows—Volume 3: Recent Advances in Numerical Methods in Fluids*, W. G. Habash, ed., Pineridge Press, 1984, pp. 281–308.
20. Delery, Jean M.: Experimental Investigation of Turbulence Properties in Transonic Shock/Boundary-Layer Interactions. *AIAA J.*, vol. 21, Feb. 1983, pp. 180–185.
21. Menter, Florian R.; and Rumsey, Christopher L.: Assessment of Two-Equation Turbulence Models for Transonic Flows. AIAA-94-2343, Jan. 1994.
22. Menter, Florian R.: *Improved Two-Equation $k-\omega$ Turbulence Models for Aerodynamic Flows*. NASA TM-103975, 1992.

23. Wilcox, David C.: Reassessment of the Scale-Determining Equation for Advanced Turbulence Models. *AIAA J.*, vol. 26, Nov. 1988, pp. 1299–1310.
24. Simpson, R. L.: A Review of Some Phenomena in Turbulent Flow Separation. *Turbulent Boundary Layers—Forced, Incompressible, Non-Reacting, Proceedings of the Joint Applied Mechanics, Fluids Engineering and Bioengineering Conference*, ASME, June 1979, pp. 1–14.
25. Agarwal, Naval K.; and Simpson, Roger L.: Backflow Structure of Steady and Unsteady Separating Turbulent Boundary Layers. *AIAA J.*, vol. 28, Oct. 1990, pp. 1764–1771.
26. Menter, F. R.: Influence of Freestream Values on $k-\omega$ Turbulence Model Predictions. *AIAA J.*, vol. 30, no. 6, June 1992, pp. 1657–1659.
27. *Experimental Data Base for Computer Program Assessment—Report of the Fluid Dynamics Panel Working Group 04*. AGARD-AR-138, May 1979.
28. Mueller, U. R.; and Henke, H.: Computation of Subsonic Viscous and Transonic Viscous-Inviscid Unsteady Flow. *Comput. & Fluids*, vol. 22, no. 4-5, July-Sept. 1993, pp. 649–661.
29. Fenno, Charles C., Jr.; Newman, Perry A.; and Hassan, H. A.: Unsteady Viscous-Inviscid Interaction Procedures for Transonic Airfoils Using Cartesian Grids. *J. Aircr.*, vol. 26, Aug. 1989, pp. 723–730.
30. Coakley, Thomas J.: Numerical Simulation of Viscous Transonic Airfoil Flows. AIAA-87-0416, Jan. 1987.
31. Barnwell, Richard W.: *Design and Performance Evaluation of Slotted Walls for Two-Dimensional Wind Tunnels*. NASA TM-78648, 1978.
32. Jenkins, Renaldo V.; and Adcock, Jerry B.: *Tables for Correcting Airfoil Data Obtained in the Langley 0.3-Meter Transonic Cryogenic Tunnel for Sidewall Boundary-Layer Effects*. NASA TM-87723, 1986.

REPORT DOCUMENTATION PAGE

Form Approved
OMB No. 0704-0188

Public reporting burden for this collection of information is estimated to average 1 hour per response, including the time for reviewing instructions, searching existing data sources, gathering and maintaining the data needed, and completing and reviewing the collection of information. Send comments regarding this burden estimate or any other aspect of this collection of information, including suggestions for reducing this burden, to Washington Headquarters Services, Directorate for Information Operations and Reports, 1215 Jefferson Davis Highway, Suite 1204, Arlington, VA 22202-4302, and to the Office of Management and Budget, Paperwork Reduction Project (0704-0188), Washington, DC 20503.

1. AGENCY USE ONLY <i>(Leave blank)</i>	2. REPORT DATE February 1998	3. REPORT TYPE AND DATES COVERED Technical Publication	
4. TITLE AND SUBTITLE Flow and Turbulence Modeling and Computation of Shock Buffet Onset for Conventional and Supercritical Airfoils		5. FUNDING NUMBERS WU 522-32-21-01	
6. AUTHOR(S) Robert E. Bartels			
7. PERFORMING ORGANIZATION NAME(S) AND ADDRESS(ES) NASA Langley Research Center Hampton, VA 23681-2199		8. PERFORMING ORGANIZATION REPORT NUMBER L-17599	
9. SPONSORING/MONITORING AGENCY NAME(S) AND ADDRESS(ES) National Aeronautics and Space Administration Washington, DC 20546-0001		10. SPONSORING/MONITORING AGENCY REPORT NUMBER NASA/TP-1998-206908	
11. SUPPLEMENTARY NOTES Bartels: NRC-NASA Resident Research Associate at Langley Research Center, Hampton, VA.			
12a. DISTRIBUTION/AVAILABILITY STATEMENT Unclassified-Unlimited Subject Category 02 Availability: NASA CASI (301) 621-0390		12b. DISTRIBUTION CODE	
13. ABSTRACT <i>(Maximum 200 words)</i> Flow and turbulence models applied to the problem of shock buffet onset are studied. The accuracy of the interactive boundary layer and the thin-layer Navier-Stokes equations solved with recent upwind techniques using similar transport field equation turbulence models is assessed for standard steady test cases, including conditions having significant shock separation. The two methods are found to compare well in the shock buffet onset region of a supercritical airfoil that involves strong trailing-edge separation. A computational analysis using the interactive-boundary layer has revealed a Reynolds scaling effect in the shock buffet onset of the supercritical airfoil, which compares well with experiment. The methods are next applied to a conventional airfoil. Steady shock-separated computations of the conventional airfoil with the two methods compare well with experiment. Although the interactive boundary layer computations in the shock buffet region compare well with experiment for the conventional airfoil, the thin-layer Navier-Stokes computations do not. These findings are discussed in connection with possible mechanisms important in the onset of shock buffet and the constraints imposed by current numerical modeling techniques.			
14. SUBJECT TERMS Shock buffet; Interactive boundary layer; Thin-layer Navier-Stokes; Two equation turbulence models; Conventional airfoils; Supercritical airfoils		15. NUMBER OF PAGES 41	16. PRICE CODE A03
17. SECURITY CLASSIFICATION OF REPORT Unclassified	18. SECURITY CLASSIFICATION OF THIS PAGE Unclassified	19. SECURITY CLASSIFICATION OF ABSTRACT Unclassified	20. LIMITATION OF ABSTRACT